nature geoscience

Article

https://doi.org/10.1038/s41561-024-01457-7

Evidence for transient morning water frost deposits on the Tharsis volcanoes of Mars

Received: 1 June 2023

Accepted: 16 April 2024

Published online: 10 June 2024

Check for updates

A. Valantinas[1,2] ✉, N. Thomas[1], A. Pommerol[1], O. Karatekin[3], L. Ruiz Lozano[3], C. B. Senel[3,4], O. Temel[3,5], E. Hauber[6], D. Tirsch[6], V. T. Bickel[7], G. Munaretto[8], M. Pajola[8], F. Oliva[9], F. Schmidt[10,11], I. Thomas[12], A. S. McEwen[13], M. Almeida[1], M. Read[1], V. G. Rangarajan[14], M. R. El-Maarry[15], C. Re[8], F. G. Carrozzo[9], E. D'Aversa[9], F. Daerden[12], B. Ristic[12], M. R. Patel[16], G. Bellucci[9], J. J. Lopez-Moreno[17], A. C. Vandaele[12] & G. Cremonese[8]

The present-day water cycle on Mars has implications for habitability and future human exploration. Water ice clouds and water vapour have been detected above the Tharsis volcanic province, suggesting the active exchange of water between regolith and atmosphere. Here we report observational evidence for extensive transient morning frost deposits on the calderas of the Tharsis volcanoes (Olympus, Arsia and Ascraeus Montes, and Ceraunius Tholus) using high-resolution colour images from the Colour and Stereo Surface Imaging System on board the European Space Agency's Trace Gas Orbiter. The transient bluish deposits appear on the caldera floor and rim in the morning during the colder Martian seasons but are not present by afternoon. The presence of water frost is supported by spectral observations, as well as independent imagery from the European Space Agency's Mars Express orbiter. Climate model simulations further suggest that early-morning surface temperatures at the high altitudes of the volcano calderas are sufficiently low to support the daily condensation of water—but not CO_2—frost. Given the unlikely seasonal nature of volcanic outgassing, we suggest the observed frost is atmospheric in origin, implying the role of microclimate in local frost formation and a contribution to the broader Mars water cycle.

The Tharsis Rise is a large volcanic province in the tropics of Mars[1] (latitude range: ±40° N, longitude range: 220–300° E). It is a broad topographic dome that rises about 5 km above the surrounding terrain and covers a region 5,000 km wide[2]. It contains some of the Solar System's largest and tallest volcanoes[3], such as Olympus Mons (21 km altitude), Arsia Mons (18 km), Ascraeus Mons (18 km) and Pavonis Mons (14 km), but also smaller shield volcanoes such as Ceraunius Tholus (9 km). Volcanic activity on Mars has been concentrated predominantly in this region throughout the planet's geological history, persisting into current times, as evidenced by lava flows that are as recent as 2.4 million years old[4]. No current volcanic activity has been detected in Tharsis, although recent geophysical data show that Mars is still geodynamically active[5–7].

Notable orographic water ice clouds and other atmospheric phenomena have been observed in Tharsis[8–12]. Water ice clouds play a fundamental role in cycling water on Mars, moving moisture for thousands of kilometres from polar regions to relatively dry equatorial areas[13,14]. In addition, Tharsis is situated along the route of an important cross-equatorial exchange of water vapour, where approximately 10^{12} kg of water is annually transferred between the northern

A full list of affiliations appears at the end of the paper. ✉e-mail: adomas_valantinas@brown.edu

https://doi.org/10.1038/s41561-024-01457-7

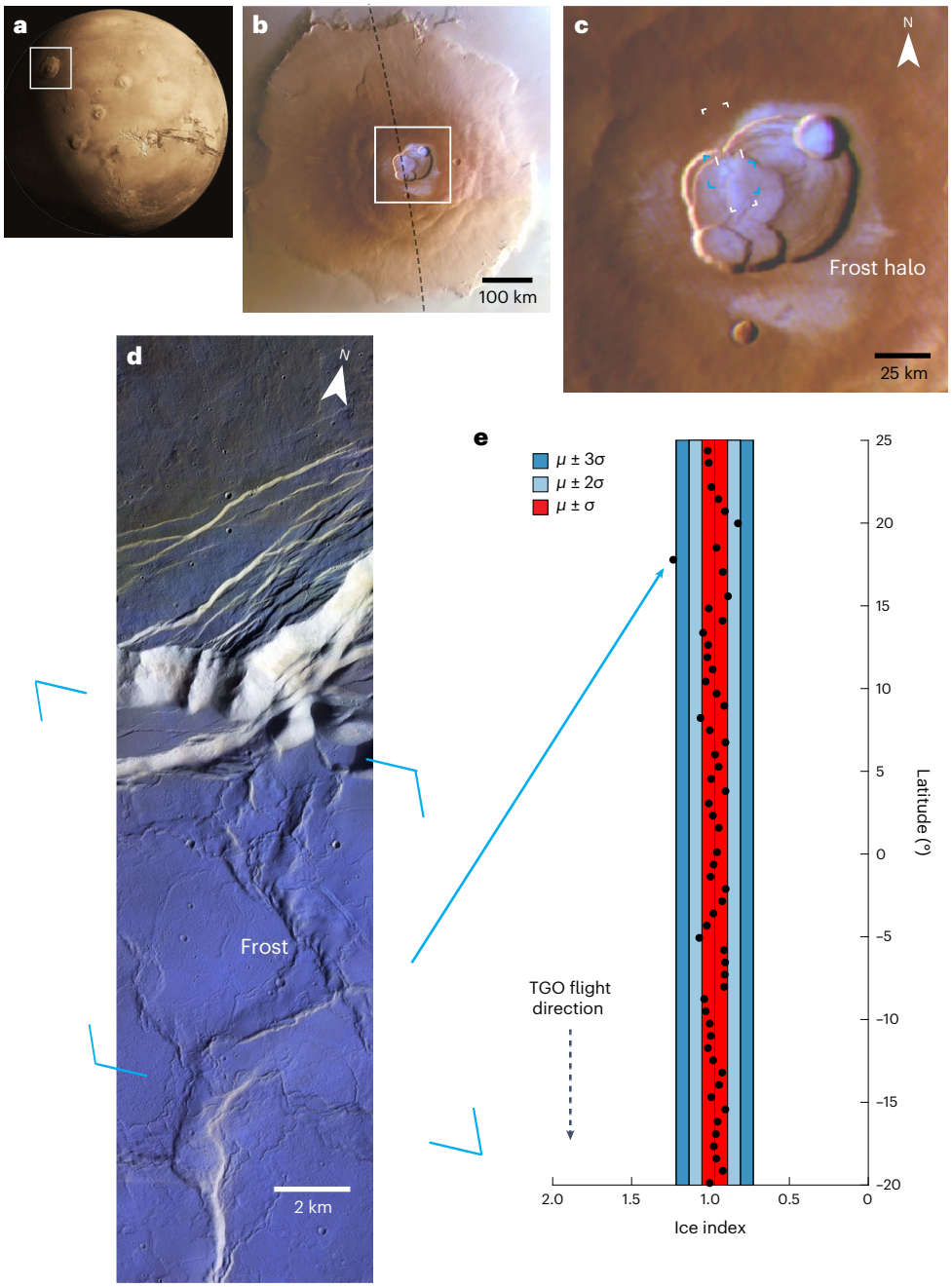

Fig. 1 | Frost detection on the Olympus Mons caldera by CaSSIS, HRSC and NOMAD. a, Global view of Mars with white box marking the location of Olympus Mons. **b**, HRSC wide-angle image of Olympus Mons acquired in the early morning (LST = 7:20, Ls = 346.7°, latitude = 18.2° N, longitude = −133.2° E). The black dashed line indicates the orbit of the TGO corresponding to the images in **d** and **e**. The white box highlights the close up in **c**. **c**, Zoomed-in view of the Olympus Mons caldera. The white and blue dashed rectangles show the footprints of the CaSSIS and NOMAD-LNO observations, respectively. **d**, High-resolution (4.5 m pixel^{-1}) CaSSIS colour image of frost on the caldera floor and northern rim of Olympus Mons (LST = 7:11, Ls = 344.1°). Frost is absent on the well-lit steep slopes. The blue rectangle marks the footprint of the one NOMAD-LNO observation that falls within the frost-covered area. **e**, NOMAD-LNO channel observation of the Olympus Mons caldera. The ice index values (Methods) indicate the presence of frost over the caldera floor (>$\mu + 3\sigma$). The coloured areas on the plot indicate the confidence intervals. HRSC image ID: hn889_0000 (**b**,**c**). CaSSIS colour image ID: MY36_022332_162_0_NPB (**d**). NOMAD-LNO observation ID: 20221125_082524 (**e**). Credit: **b**, ESA/DLR/FU Berlin; **d**, ESA/TGO/CaSSIS under a Creative Commons license CC-BY-SA 3.0 IGO.

and southern hemispheres through the solstitial Hadley cells[15]. Atmospheric observations[16] have revealed a localized enrichment in water vapour above the Tharsis volcanoes, suggesting that an active exchange of water vapour between the regolith and the atmosphere may be ongoing, probably facilitated by desorption from the regolith and/or sublimation of frost. A subsequent study[17] confirmed the water-vapour enrichment over these areas but hypothesized that the local circulation pattern typical of the volcanic region is possibly responsible for the enrichment as it may carry considerable amounts of water vapour upslope.

Apart from the polar regions, water ice manifests on the surface as seasonal frost in mid- and low-latitude locations. NASA's (the National Aeronautics and Space Administration's) Viking 2 lander detected water frost at ~48° N[18–20]. In addition, orbital observations from a variety of instruments revealed that water frost can occur up to 13° S in the southern hemisphere and as low as 32° N on shaded

https://doi.org/10.1038/s41561-024-01457-7

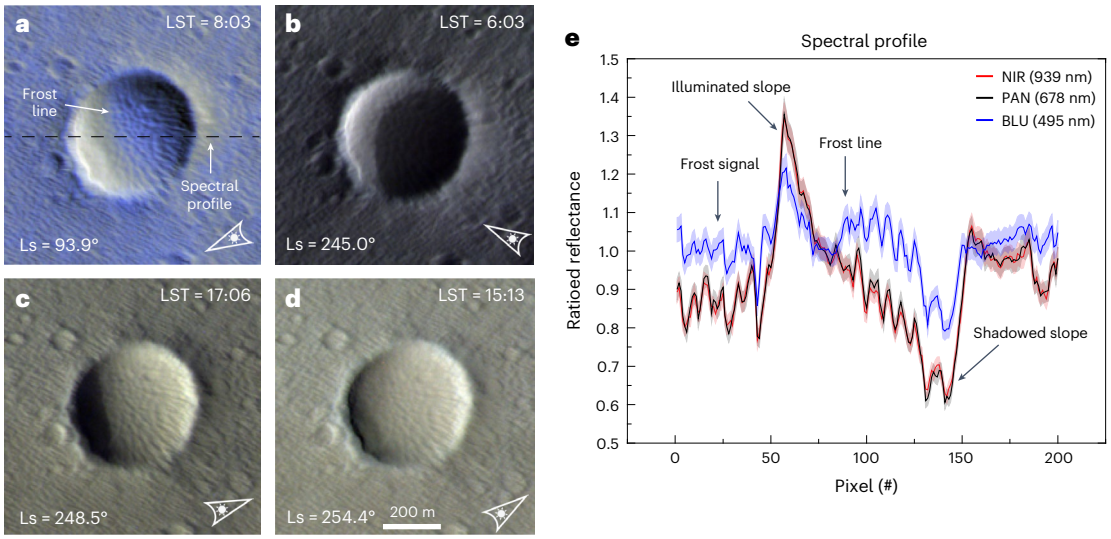

Fig. 2 | Frost occurrence on a crater in the Arsia Mons caldera. a, Frost on the shadowed slope of the crater in an early-morning observation during southern winter in MY 35 (latitude = −8.74° N, longitude = −121.14° E). **b**–**d**, No frost in an early-morning observation (**b**) and no frost in afternoon observations (**c**,**d**) during late southern spring in MY 36. The spectral profile along the black line in **a** is shown in **e** and reveals a marked increase in reflectance up to 20% in the BLU filter when frost is present. Errors are from the uncertainty in the absolute calibration of the instrument and are about ~3% (ref. 43). The illumination direction is indicated by the arrows in the bottom right corner of each image. North is up in all panels. The CaSSIS image IDs are shown in order (**a**–**d**): MY35_008465_192_0_NPB, MY36_020297_350_3_NPB, MY36_020366_190_1_NPB and MY36_020478_190_3_NPB. Credit: **a**, ESA/TGO/CaSSIS under a Creative Commons license CC-BY-SA 3.0 IGO.

pole-facing slopes[21–23]. However, the presence of frost at the tropics (~0° N latitude) was not expected because of higher average surface temperatures[24] and lower humidity[25]. Some studies predicted that on most of Mars's surface, small amounts of H_2O frost can condense nightly if radiative cooling is strong enough[26,27]. For example, extremely small amounts of water frost have been observed to condense near the equator on the high thermal emissivity calibration targets of NASA's Opportunity rover[28,29].

Most of the Martian atmosphere is composed of CO_2 gas, and therefore CO_2 frost can also form if surface temperatures are low enough[30]. On the basis of nightly surface temperatures and thermal modelling, it was shown that in the equatorial regions CO_2 frost may condense diurnally[29–32]. Predictions[30,31] indicated that putative CO_2 frost deposits may persist for only a few minutes after sunrise (~6:00 Local Solar Time (LST)) before sublimating back into the atmosphere. Follow-up global surveys, utilizing early-morning colour observations from the Thermal Emission Imaging System (THEMIS[33]) were conducted to search for these frosts in the equatorial regions, but no evidence of morning CO_2 frost was identified[34].

Observations by the Colour and Stereo Surface Imaging System (CaSSIS[35]) on board the European Space Agency's (ESA's) Trace Gas Orbiter (TGO) provide strong evidence for morning frost deposition on the equatorial Tharsis volcanoes. We present here these observations coupled with supporting evidence from other instruments and modelling.

Observations of frost

Early-morning images (LST = 7:11; latitude = 18.5° N, longitude = −133.5° E; spatial resolution = 4.5 m pixel^{-1}) of Olympus Mons caldera acquired by CaSSIS (at UTC 2022 November 25) in the late northern winter (solar longitude (Ls) ~345°) on Mars year (MY) 36 first revealed bluish deposits (at ~500 nm) on sections of the caldera floor and rim (Fig. 1). The CaSSIS observation suggests a spatial correlation between the bluish deposits and topography (Fig. 1d). The deposits are concentrated on the caldera floor but are absent on well-illuminated warm slopes and farther north on the volcano flank. The finding was confirmed five days later with a High Resolution Stereo Camera (HRSC)[36] observation acquired on 2022 November 30 (LST = 7:20; latitude = 18.2° N, longitude = −133.2° E; spatial resolution = 800 m pixel^{-1}), which revealed that the diffuse bluish 'halo' deposit was ubiquitous on the entire caldera floor and rim (Fig. 1b,c). The halo is absent on the volcano flanks and is concentrated only at the mountain summit. During the CaSSIS detection, the Nadir and Occultation for Mars Discovery (NOMAD[37]) spectrometer was operating and acquired a ride-along observation (instantaneous field of view = 17.5 km × 0.5 km). The nadir spectral data acquired in the NOMAD limb nadir and solar occultation (LNO) channel revealed that the deposit is frost (Fig. 1e) as indicated by the elevated ice index values (more than 3σ confidence; Methods and Supplementary Figs. 1 and 2).

Repeat imaging by HRSC shows that the frost deposits on top of Olympus Mons (Fig. 1b) appear only in the early Martian morning (LST = ~7:00–7:30; latitude = 18.2° N, longitude = −133.2° E) and are spatially correlated with a geological bright halo unit (Extended Data Fig. 1a,d). This unit may be dust that is relatively brighter than the surrounding material due to different grain size or texture[38]. This bright halo unit is also observed in Context Camera[39] images (Extended Data Fig. 2a). Materials consisting of smaller particles may exhibit different thermophysical properties such as lower thermal conductivity[40] and high thermal emissivity[41]. Surfaces with such properties cool down more at night and warm up more slowly in the morning, further enhancing the likelihood and duration of frost formation. This latter point is illustrated by CaSSIS observations of frost on dust deposits that have not been removed by winds (Extended Data Fig. 2b,c). As shown by CaSSIS, frost may also condense leeward of small craters where air-fall dust can accumulate and is perhaps less compact (Extended Data Fig. 2d). Porous and less-compact materials provide more nucleation sites for frost formation[42]. Outside of the bright halo, frost is found near the northern rim of Olympus Mons, but its emplacement is more localized (Extended Data Fig. 2e–i). In conclusion, the observed frost patterns on Olympus Mons, particularly in areas with geologically distinct bright dust deposits, underscore the importance of thermophysical properties such as low thermal conductivity and high thermal emissivity, as well as surface texture, in governing the formation, distribution and persistence of frost on Mars.

https://doi.org/10.1038/s41561-024-01457-7

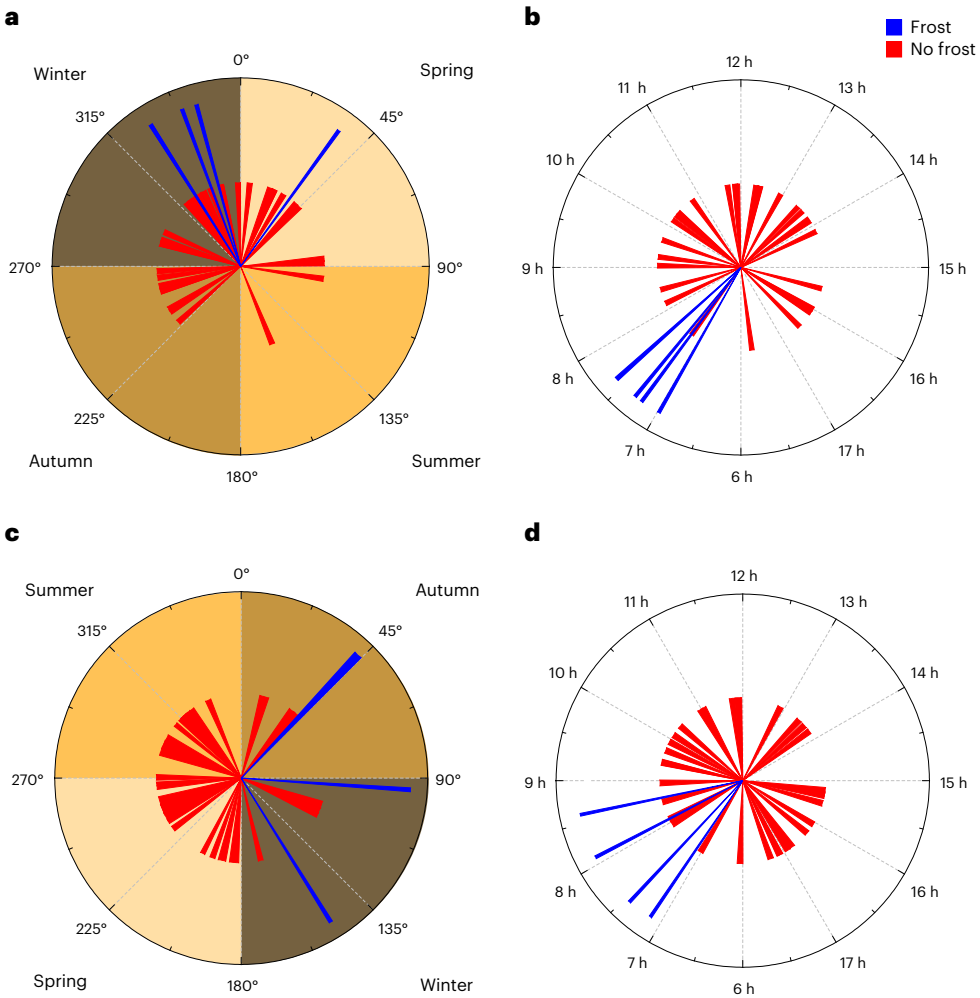

Fig. 3 | Seasonal and diurnal trends of frost on Olympus and Arsia Montes. **a**–**d**, Rose diagrams showing the seasonal (**a**,**c**) and diurnal (**b**,**d**) frost detections by CaSSIS over Olympus Mons (**a**,**b**) and Arsia Mons (**c**,**d**). The width of each bin reflects the number of CaSSIS observations. Frost is detected around northern spring equinox (Ls = ~0°) on Olympus Mons and around southern winter solstice (Ls = ~90°) on Arsia Mons. Frost is detected only in the early-morning hours (~7:00–8:00 LST). The negative detections in the early morning bins correspond to observations that were acquired in warmer seasons.

Within the CaSSIS database, 13 instances of frost have been found (Extended Data Fig. 3). These include detections not only on the largest Tharsis volcanoes of Olympus, Ascraeus and Arsia Montes but also on the smaller-sized Ceraunius Tholus shield volcano (Extended Data Fig. 4). In one case, the frost deposits on Arsia Mons (Fig. 2a) are observed in the early Martian morning and during southern winter solstice (LST = ~8:00, Ls = ~90°, latitude = −8.7° N, longitude = −121.1° E). The frost line dividing warm and shadowed slopes is, however, not observed in the repeat CaSSIS observations of this location, which were acquired during late southern spring (Fig. 2b–d). Photometric analysis shows that frost is associated with an increase in ratioed reflectance of up to 20% at wavelengths (Fig. 2e; CaSSIS blue (BLU) filter bandwidth is 390–570 nm (ref. 43)). The fact that frosty surfaces are sometimes brighter only at blue wavelengths, implying a lower spectral slope, can also be observed in a linearly stretched CaSSIS BLU filter image (Extended Data Fig. 5 and Methods) and average spectra from a *k*-means clustering analysis[44,45] applied on a topographically corrected and photometrically normalized CaSSIS cube (Supplementary Fig. 3). The photometric and clustering analyses suggest that the frost deposits are probably very thin.

CaSSIS observations of Olympus and Arsia Montes indicate diurnal and possibly seasonal trends in frost deposition (Fig. 3). The four detections in Olympus Mons (Fig. 3a,b) are clustered around the early-morning hours (LST = ~7:00–7:30) and northern spring equinox (Ls = ~320–40°). Similarly, the four detections in Arsia Mons (Fig. 3c–d) fall within a slightly wider time range (LST = ~7:00–8:30) but around the southern winter solstice (Ls = ~45–145°). The early-morning non-detections in Arsia Mons fall within the southern summer period, which suggests seasonality (Extended Data Fig. 6b), but the lack of early-morning observations in the northern summer precludes us from making the same conclusion for the detections in Olympus Mons (Extended Data Fig. 6a). We removed observations at extremely high solar incidence angles (>85°) because of low image signal-to-noise ratio (SNR), and therefore there is an observational bias towards LSTs at about 6:00 (Methods). Collectively, CaSSIS observations suggest that the frost cycle over Martian volcanoes is ephemeral and exhibits variability on multiple timescales. It appears to be influenced by diurnal patterns, probably reflecting daily temperature fluctuations. In addition, there is a probable control by the Martian seasons, indicating a longer-term variation in the frost cycle. On the basis of the CaSSIS observations, while there are indications of diurnal and seasonal influences on frost deposition on Martian volcanoes, these observations alone cannot definitively determine the composition of the frost. Therefore, we use simulations of surface temperatures as a proxy for frost composition.

Surface temperatures indicate water frost

At the time of CaSSIS frost detections in Olympus Mons (Fig. 1) and Arsia Mons (Fig. 2), the surface temperatures calculated by the general

https://doi.org/10.1038/s41561-024-01457-7

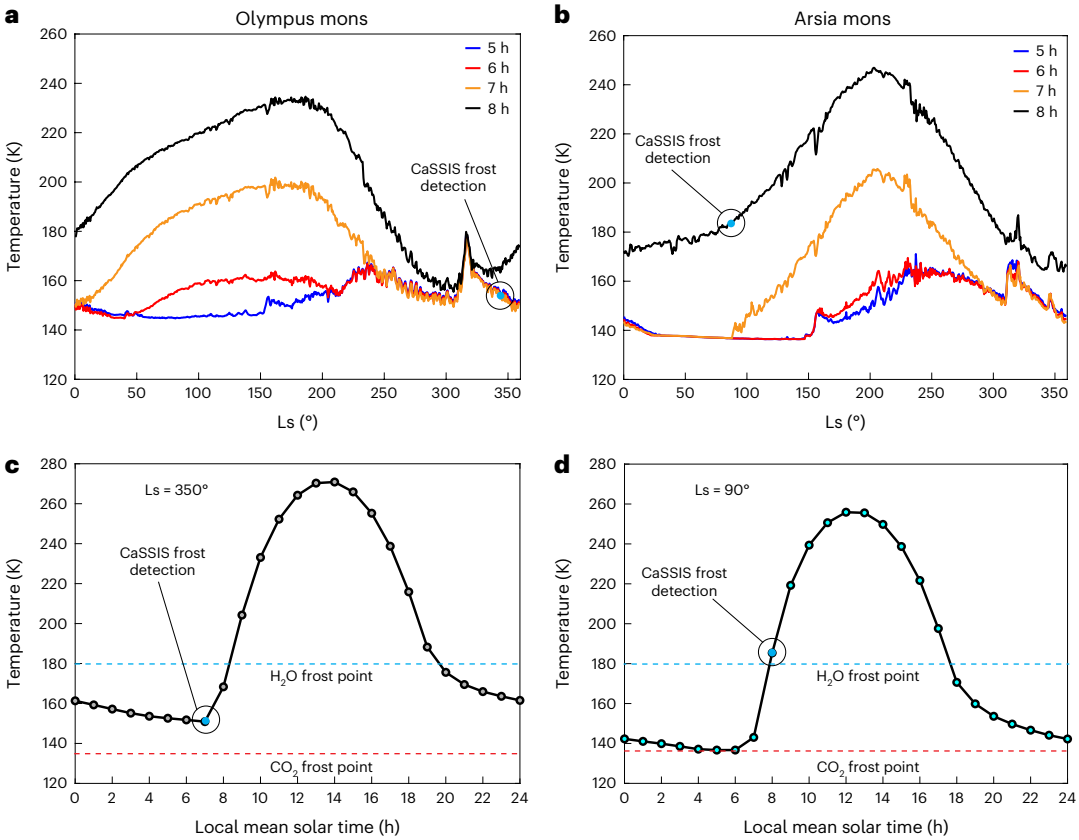

Fig. 4 | Modelled surface temperatures at Olympus Mons and Arsia Mons. **a**,**b**, Annual surface temperatures at four different local mean solar times (LMST). **c**,**d**, Diurnal surface temperatures at Olympus Mons (Ls = 350°) (**c**) and Arsia Mons (Ls = 90°) (**d**) as predicted by the GCM. In **c**,**d**, blue and red horizontal dashed lines depict CO_2[30] and H_2O frost point[14], respectively. On both volcano calderas at the time of CaSSIS image acquisition, CO_2 frost point is not reached. This indicates favourable conditions for H_2O ice. The simulations were conducted at geographical coordinates 18.75° N, −133.75° E for Olympus Mons and −8.75° N, −121.25 °E for Arsia Mons.

circulation model (GCM[46]) via the Mars Weather Research and Forecasting (WRF[47]) model are inconsistent with CO_2 frost. The stability of CO_2 frost at higher altitudes necessitates exceptionally low temperatures, specifically below 140 K, to maintain its solid state[30]. The predicted surface temperatures (at ~150 km model resolution) are ~150 K and 185 K at ~7:00 LST in Olympus Mons and at ~8:00 LST in Arsia Mons, respectively (Fig. 4). In addition, advanced high-resolution mesoscale modelling, with a model resolution of 5.47 km, reveals a substantial temperature difference between the surface temperature and the local CO_2 frost point at the locations of CaSSIS observations, with a difference of approximately 10 K at Olympus Mons (Fig. 5d) and over 55 K at Arsia Mons (Extended Data Fig. 7d). In fact, the surface temperatures predicted at each CaSSIS frost location (Table 1) consistently exceed the CO_2 frost point, corresponding to the mean surface temperature ~162 K (excluding C3 and C6). The stratification of water vapour in Mars's atmosphere, especially near the surface, is not well understood[48], making the determination of the H_2O frost point challenging due to its considerable variability; however, it is generally accepted that this point occurs at around 180 K (ref. 14). Since the predicted surface temperatures at the time of CaSSIS, HRSC and NOMAD observations are too warm, this suggests that CO_2 frost is unlikely, hence providing support for the presence of water frost. At these seasons (Ls = 346.7° for Olympus Mons and Ls = 93.8° for Arsia Mons), CO_2 frost was also not observed by the Thermal Emission Imaging System[29] or by the Emirates Mars InfraRed Spectrometer[32]. Interestingly, the GCM also predicts that some CO_2 frost may be present at Ls = ~0–150° and at around sunrise (5:00–6:00 LST) in Arsia Mons (Fig. 4b). This result is consistent with previous studies indicating CO_2 frost formation from minutes to tens of minutes after sunrise in the equatorial regions[29–31]. However, such potential CO_2 frost deposits would sublime very quickly and would be difficult to detect by cameras and spectrometers due to low SNR[34]. In addition, we investigated the possible role of CO_2 frost in regolith gardening and slope streak formation on Mars[30,34,49]. We found no slope streaks on the calderas of the largest Tharsis volcanoes or any obvious differences in talus boulder shapes and sizes (Methods and Extended Data Fig. 8). These results suggest that the diurnal CO_2 or H_2O frost cycle plays a minor (if any) role in landscape evolution at these sites.

Microclimate and water ice amount

Our high-resolution mesoscale simulations reveal the distinct microclimatic conditions induced by the topography of the Tharsis volcanoes, as shown in Fig. 5 and Extended Data Fig. 7. Specifically, within the calderas of Olympus Mons and Arsia Mons, we observe a substantial reduction in surface atmospheric pressure and near-surface horizontal wind speeds compared with the surrounding areas. For example, within the caldera of Olympus Mons (Fig. 5b), the atmospheric pressure is estimated at only 110 Pa, compared with 160 Pa at the mountain's base. Similarly, in the area of Arsia Mons (Extended Data Fig. 7b), the pressure is about 100 Pa, notably lower than the over 200 Pa found in the adjacent plains. Moreover, the near-surface horizontal wind speeds within Olympus Mons (Fig. 5c) are estimated at less than 10 m s^{-1}, in stark contrast to the approximately 30 m s^{-1} observed along the volcano's flanks. In the case of Arsia Mons (Extended Data Fig. 7c), the wind speeds are below 5 m s^{-1} within the caldera, compared with roughly 20 m s^{-1} on the flanks, highlighting the profound impact of volcanic topography on localized weather patterns.

https://doi.org/10.1038/s41561-024-01457-7

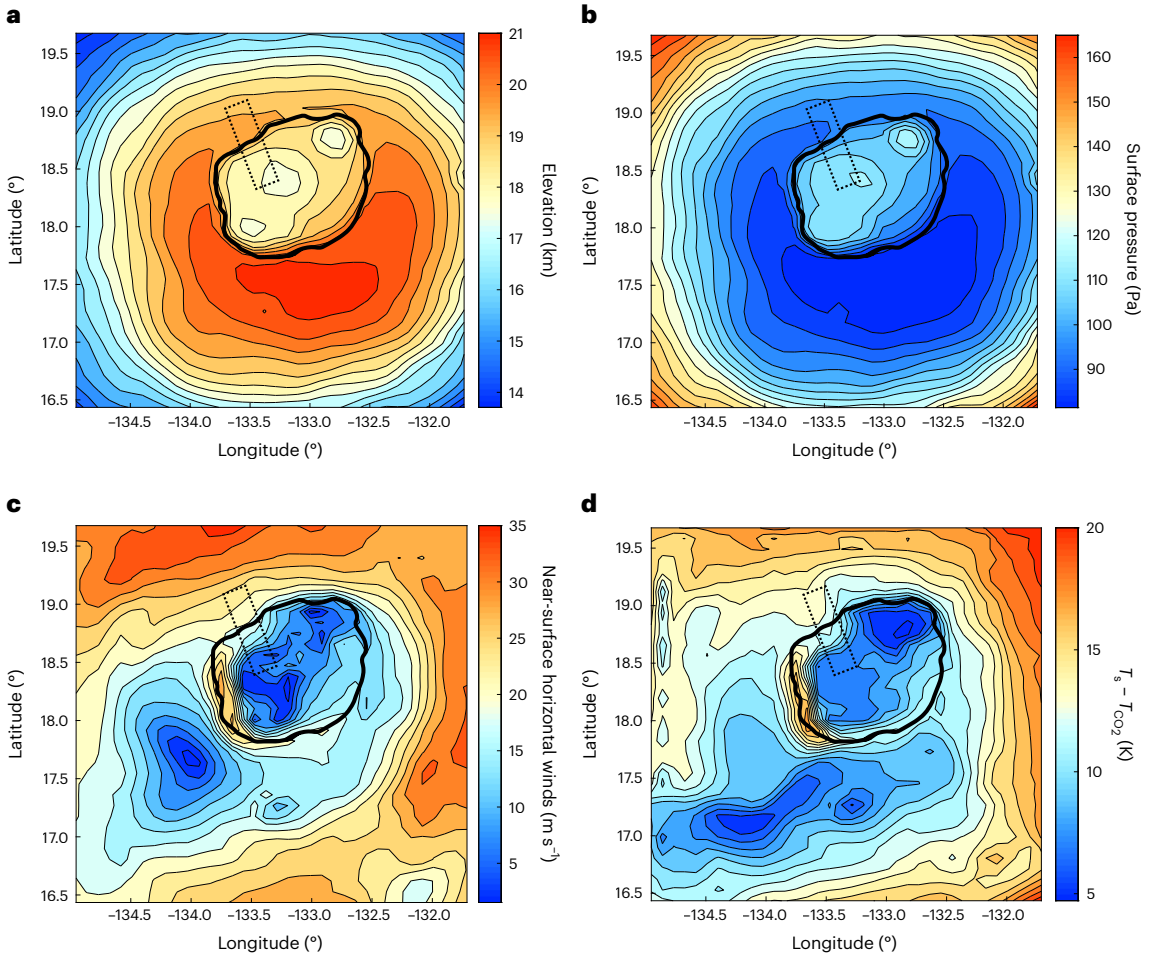

Fig. 5 | Microclimatic conditions simulated over Olympus Mons. **a**–**d**, Utilizing MarsWRF high-resolution mesoscale modelling (at the time of CaSSIS observation Fig. 1d), this figure presents the influence of Olympus Mons's topography on its local climate, as shown by elevation gradients (**a**), surface atmospheric pressure (**b**), near-surface horizontal wind patterns (**c**) and the deviation in temperature between the Martian surface and the local CO_2 frost point (**d**). The topography of the Olympus Mons caldera is demonstrated to cause noticeable variations in local pressure, wind velocities and temperature gradients. The black outline across all panels highlights the boundary of the Olympus Mons caldera, while the black dashed rectangle marks the area observed by CaSSIS, as referenced in Fig. 1d. The CO_2 frost point in the area of CaSSIS observation is exceeded by about 10 K. By contrast, the CO_2 frost point in Arsia Mons is exceeded by around 60 K (Extended Data Fig. 7d).

Table 1 | CaSSIS frost detection times and predicted surface temperatures by the GCM

ID	Locality	Ls (°)	LST (h)	Estimated surface temperature (K)	Estimated CO_2 frost temperature (K)	Estimated surface pressure (Pa)	H_2O ice stability?
C1	Olympus Mons	326.98	7:35	160.83	136.83	114.03	Yes
C2	Arsia Mons	93.94	8:04	186.83	136.81	113.60	Yes
C3	Arsia Mons	148.07	7:25	216.70	136.77	112.83	[a]
C4	Olympus Mons	338.96	7:17	156.77	136.69	111.34	Yes
C5	Olympus Mons	35.24	6:58	164.34	136.58	109.35	Yes
C6	Arsia Mons	43.39	8:35	215.77	137.90	136.63	[a]
C7	Ascraeus Mons	35.20	7:06	162.75	138.41	148.78	Yes
C8	Olympus Mons	344.08	7:12	153.04	136.67	110.98	Yes
C9	Ceraunius Tholus	16.82	7:05	No data	No data	No data	No data
C10	Ascraeus Mons	42.80	7:20	166.16	138.31	146.19	Yes
C11	Arsia Mons	44.19	7:08	155.19	138.68	155.59	Yes
C12	Olympus Mons	18.80	6:10	147.07	136.61	109.79	Yes
C13	Olympus Mons	42.84	7:13	170.53	136.55	108.69	Yes

[a]Frost is found only on shadowed slopes.

Furthermore, our GCM simulations suggest that the thickness of water frost deposits is on the order of 1 µm (Methods). However, this estimate carries considerable uncertainty due to the unknown quantities of water-vapour-column abundances. To refine this estimate, we reference radiative transfer calculations[50,51], which suggest a minimum thickness of 100 µm, while laboratory experiments[52] imply a thickness of about 10 µm (Methods). By adopting the median thickness of 10 µm for the water frost, and considering that the frost deposits are confined to the calderas of Olympus, Arsia, Ascraeus Montes and Ceraunius Tholus, we estimate that there is a transfer of approximately 1.5×10^8 kg of water ice between the surface and the atmosphere (Methods).

Possible sources of water vapour

The seasonal trends as shown by the set ($n = 13$) of CaSSIS observations suggests an atmospheric phenomenon driven by water transport due to large-scale seasonal changes, such as sublimation of the seasonal ice cap in the opposite hemisphere and transportation of humid air into the volcano calderas by upslope winds. Seasonal processes have been observed at a wide range of Martian latitudes[53] and may also apply to the Tharsis region. For example, the activity of the Aphelion Cloud Belt peaks at Ls ~40°–140° (ref. 54), and in general little cloud activity is observed at Ls ~245°–320°[10]. Similarly, afternoon orographic clouds have been detected by Mars Reconnaissance Orbiter's Mars Color Imager[55] over the Tharsis volcanoes[10]. The seasonal observation of water-vapour enrichment over Tharsis[17] shows increased abundances around northern spring equinox (Ls 0°), consistent with the CaSSIS detections of frost close to this season in Olympus Mons. Therefore, we hypothesize that this water-vapour enrichment[17] may be the source of the frost deposits detected in our study. The transport of water vapour from high latitudes to the Tharsis highlands could be facilitated by large-scale atmospheric eddies[56]. This process could be further augmented by strong upslope winds, driven by a combination of thermal effects and mountain gravity waves[57], facilitating the movement of moisture over the volcano calderas. The local topography-induced circulation[57] and microclimatic conditions within the caldera (shown in Fig. 5 and Extended Data Fig. 7) may create favourable conditions for water frost condensation during the cold Martian nights. Within these calderas, ~150,000 tons of water ice is exchanged daily between the regolith and the atmosphere during the cold Martian seasons. Although this amount is relatively a small fraction of the seasonal inventory of water vapour in the Martian atmosphere (~10^{12} kg) (ref. 14), it is important in the context of localized Martian environmental processes. Understanding these micro-environments is crucial for a comprehensive understanding of Mars's hydrological cycle.

It is conceivable that dormant volcanoes can emit CO_2, water vapour and minor amounts of SO_2 (ref. 58) via diffuse outgassing from the regolith[59,60]. If the observed water frost deposits are of volcanic origin, their distribution may constrain models for present-day outgassing from the interior. However, on Mars, SO_2 has not been detected[61] and no thermal hotspots have been found[62]. A volcanic source for the condensate cannot completely be ruled out, but further tests for trace species (CO_2, H_2S and SO_2) would be useful to explore the likelihood of this potential mechanism. Consequently, we conclude here that the newly detected frosts on Tharsis volcano calderas are probably of atmospheric origin.

Online content

Any methods, additional references, Nature Portfolio reporting summaries, source data, extended data, supplementary information, acknowledgements, peer review information; details of author contributions and competing interests; and statements of data and code availability are available at https://doi.org/10.1038/s41561-024-01457-7.

References

1. Carr, M. H. Tectonism and volcanism of the Tharsis region of Mars. *J. Geophys. Res.* **79**, 3943–3949 (1974).
2. Smith, D. E. et al. Mars Orbiter Laser Altimeter: experiment summary after the first year of global mapping of Mars. *J. Geophys. Res. Planets* **106**, 23689–23722 (2001).
3. Plescia, J. B. Morphometric properties of Martian volcanoes. *J. Geophys. Res. Planets* **109**, E03003 (2004).
4. Neukum, G. et al. Recent and episodic volcanic and glacial activity on Mars revealed by the High Resolution Stereo Camera. *Nature* **432**, 971–979 (2004).
5. Giardini, D. et al. The seismicity of Mars. *Nat. Geosci.* **13**, 205–212 (2020).
6. Stähler, S. C. et al. Tectonics of Cerberus Fossae unveiled by marsquakes. *Nat. Astron.* **6**, 1376–1386 (2022).
7. Broquet, A. & Andrews-Hanna, J. C. Geophysical evidence for an active mantle plume underneath Elysium Planitia on Mars. *Nat. Astron.* **7**, 160–169 (2023).
8. Curran, R. J., Conrath, B. J., Hanel, R. A., Kunde, V. G. & Pearl, J. C. Mars: Mariner 9 spectroscopic evidence for H_2O ice clouds. *Science* **182**, 381–383 (1973).
9. Kahn, R. The spatial and seasonal distribution of Martian clouds and some meteorological implications. *J. Geophys. Res. Space Phys.* **89**, 6671–6688 (1984).
10. Benson, J. L., James, P. B., Cantor, B. A. & Remigio, R. Interannual variability of water ice clouds over major Martian volcanoes observed by MOC. *Icarus* **184**, 365–371 (2006).
11. Hernández-Bernal, J. et al. An extremely elongated cloud over Arsia Mons volcano on Mars: I. Life cycle. *J. Geophys. Res. Planets* **126**, e2020JE006517 (2021).
12. Fernando, A. M., Wolff, M. J. & Forget, F. Seasonal variations of orographic clouds on Mars with MRO/MARCI observations and the Mars Planetary Climate Model. *Icarus* **400**, 115559 (2023).
13. Houben, H., Haberle, R. M., Young, R. E. & Zent, A. P. Modeling the Martian seasonal water cycle. *J. Geophys. Res. Planets* **102**, 9069–9083 (1997).
14. Montmessin, F., Smith, M. D., Langevin, Y., Mellon, M. T. & Fedorova, A. in *The Atmosphere and Climate of Mars* (eds Clancy, R. T. et al.) 338–373 (Cambridge Univ. Press, 2017); https://doi.org/10.1017/9781139060172.011
15. Montmessin, F., Forget, F., Rannou, P., Cabane, M. & Haberle, R. M. Origin and role of water ice clouds in the Martian water cycle as inferred from a general circulation model. *J. Geophys. Res. Planets* **109**, E10004 (2004).
16. Titov, D. V. et al. Observations of water vapour anomaly above Tharsis volcanoes on Mars in the ISM (Phobos-2) experiment. *Planet. Space Sci.* **42**, 1001–1010 (1994).
17. Maltagliati, L. et al. Observations of atmospheric water vapor above the Tharsis volcanoes on Mars with the OMEGA/MEx imaging spectrometer. *Icarus* **194**, 53–64 (2008).
18. Jones, K. L. et al. One Mars year: Viking lander imaging observations. *Science* **204**, 799–806 (1979).
19. Hart, H. M. & Jakosky, B. M. Composition and stability of the condensate observed at the Viking lander 2 site on Mars. *Icarus* **66**, 134–142 (1986).
20. Svitek, T. & Murray, B. Winter frost at Viking lander 2 site. *J. Geophys. Res. Solid Earth* **95**, 1495–1510 (1990).
21. Carrozzo, F. G., Bellucci, G., Altieri, F., D'Aversa, E. & Bibring, J.-P. Mapping of water frost and ice at low latitudes on Mars. *Icarus* **203**, 406–420 (2009).
22. Schorghofer, N. & Edgett, K. S. Seasonal surface frost at low latitudes on Mars. *Icarus* **180**, 321–334 (2006).
23. Vincendon, M. et al. Near-tropical subsurface ice on Mars. *Geophys. Res. Lett.* **37**, L01202 (2010).
24. Piqueux, S. et al. Mars thermal inertia and surface temperatures by the Mars Climate Sounder. *Icarus* https://doi.org/10.1016/j.icarus.2023.115851 (2023).

25. Fedorova, A. et al. Mars water vapor abundance from SPICAM IR spectrometer: seasonal and geographic distributions. *J. Geophys. Res. Planets* **111**, E09S08 (2006).
26. Davies, D. W. The relative humidity of Mars' atmosphere. *J. Geophys. Res. Solid Earth* **84**, 8335–8340 (1979).
27. Jakosky, B. M. The seasonal cycle of water on Mars. *Space Sci. Rev.* **41**, 131–200 (1985).
28. Landis, G. A. Observation of frost at the equator of Mars by the Opportunity rover. In *Proc. 38th Annu. Lunar Planet. Sci. Conf.* abstr. 2433 (2007).
29. Khuller, A. R., Christensen, P. R., Harrison, T. N. & Diniega, S. The distribution of frosts on Mars: links to present-day gully activity. *J. Geophys. Res. Planets* **126**, e2020JE006577 (2021).
30. Piqueux, S. et al. Discovery of a widespread low-latitude diurnal CO_2 frost cycle on Mars. *J. Geophys. Res. Planets* **121**, 1174–1189 (2016).
31. Cushing, G. E. & Titus, T. N. MGS-TES thermal inertia study of the Arsia Mons caldera. *J. Geophys. Res. Planets* **113**, E06006 (2008).
32. Stcherbinine, A. et al. Diurnal and seasonal mapping of Martian ices with EMIRS. *Geophys. Res. Lett.* **50**, e2023GL103629 (2023).
33. Christensen, P. R. et al. in *2001 Mars Odyssey* (ed. Russell, C. T.) 85–130 (Springer, 2004); https://doi.org/10.1007/978-0-306-48600-5_3
34. Lange, L., Piqueux, S. & Edwards, C. S. Gardening of the Martian regolith by diurnal CO_2 frost and the formation of slope streaks. *J. Geophys. Res. Planets* **127**, e2021JE006988 (2022).
35. Thomas, N. et al. The Colour and Stereo Surface Imaging System (CaSSIS) for the ExoMars Trace Gas Orbiter. *Space Sci. Rev.* **212**, 1897–1944 (2017).
36. Neukum, G., Jaumann, R. & the HRSC Co-Investigator and Experiment Team. HRSC: the high resolution stereo camera of Mars Express. *ESA* **1240**, 17–35 (2024).
37. Vandaele, A. C. et al. NOMAD, an integrated suite of three spectrometers for the ExoMars Trace Gas Mission: technical description, science objectives and expected performance. *Space Sci. Rev.* **214**, 80 (2018).
38. Hapke, B. *Theory of Reflectance and Emittance Spectroscopy* (Cambridge Univ. Press, 2012); https://doi.org/10.1017/CBO9781139025683
39. Malin, M. C. et al. Context Camera Investigation on board the Mars Reconnaissance Orbiter. *J. Geophys. Res. Planets* **112**, E05S04 (2007).
40. Presley, M. & Christensen, P. Thermal conductivity measurements of particulate materials: 4. Effect of bulk density for granular particles. *J. Geophys. Res.* **115**, E07003 (2010).
41. Christensen, P. R. Martian dust mantling and surface composition: interpretation of thermophysical properties. *J. Geophys. Res. Solid Earth* **87**, 9985–9998 (1982).
42. Presley, M. A. & Christensen, P. R. Thermal conductivity measurements of particulate materials 2. Results. *J. Geophys. Res. Planets* **102**, 6551–6566 (1997).
43. Thomas, N. et al. Absolute calibration of the Colour and Stereo Surface Imaging System (CaSSIS). *Planet. Space Sci.* **211**, 105394 (2022).
44. Marzo, G. A., Roush, T. L., Blanco, A., Fonti, S. & Orofino, V. Cluster analysis of planetary remote sensing spectral data. *J. Geophys. Res. Planets* **111**, E03002 (2006).
45. Pajola, M. et al. Lermontov crater on Mercury: geology, morphology and spectral properties of the coexisting hollows and pyroclastic deposits. *Planet. Space Sci.* **195**, 105136 (2021).
46. Senel, C. B. et al. Interannual, seasonal and regional variations in the Martian convective boundary layer derived from GCM simulations with a semi-interactive dust transport model. *J. Geophys. Res. Planets* **126**, e2021JE006965 (2021).
47. Richardson, M. I., Toigo, A. D. & Newman, C. E. PlanetWRF: a general purpose, local to global numerical model for planetary atmospheric and climate dynamics. *J. Geophys. Res. Planets* **112**, E09001 (2007).
48. Tamppari, L. K. & Lemmon, M. T. Near-surface atmospheric water vapor enhancement at the Mars Phoenix lander site. *Icarus* **343**, 113624 (2020).
49. Valantinas, A. et al. CaSSIS color and multi-angular observations of Martian slope streaks. *Planet. Space Sci.* **209**, 105373 (2021).
50. Wiscombe, W. J. & Warren, S. G. A model for the spectral albedo of snow. I: pure snow. *J. Atmos. Sci.* **37**, 2712–2733 (1980).
51. Khuller, A. R., Christensen, P. R. & Warren, S. G. Spectral albedo of dusty Martian H_2O snow and ice. *J. Geophys. Res. Planets* **126**, e2021JE006910 (2021).
52. Spadaccia, S., Patty, C. H. L., Thomas, N. & Pommerol, A. Experimental study of frost detectability on planetary surfaces using multicolor photometry and polarimetry. *Icarus* **396**, 115503 (2023).
53. Dundas, C. M. et al. Active Mars: a dynamic world. *J. Geophys. Res. Planets* **126**, e2021JE006876 (2021).
54. Clancy, R. T. et al. in *The Atmosphere and Climate of Mars* (eds. Clancy, R. T. et al.) 76–105 (Cambridge Univ. Press, 2017); https://doi.org/10.1017/9781139060172.005
55. Bell, J. F. III et al. Mars Reconnaissance Orbiter Mars Color Imager (MARCI): instrument description, calibration, and performance. *J. Geophys. Res. Planets* **114**, E08S92 (2009).
56. Greybush, S. J., Gillespie, H. E. & Wilson, R. J. Transient eddies in the TES/MCS Ensemble Mars Atmosphere Reanalysis System (EMARS). *Icarus* **317**, 158–181 (2019).
57. Rafkin, S. C. R., Sta. Maria, M. R. V. & Michaels, T. I. Simulation of the atmospheric thermal circulation of a Martian volcano using a mesoscale numerical model. *Nature* **419**, 697–699 (2002).
58. Symonds, R. B., Rose, W. I., Bluth, G. J. S. & Gerlach, T. M. in *Volatiles in Magmas* (eds. Carroll, M. R. & Holloway, J. R.) 1–66 (De Gruyter, 1994); https://doi.org/10.1515/9781501509674-007
59. Hernández, P. et al. Soil gas CO_2, CH_4, and H_2 distribution in and around Las Cañadas caldera, Tenerife, Canary Islands, Spain. *J. Volcanol. Geotherm. Res.* **103**, 425–438 (2000).
60. Chiodini, G. et al. Fumarolic and diffuse soil degassing west of Mount Epomeo, Ischia, Italy. *J. Volcanol. Geotherm. Res.* **133**, 291–309 (2004).
61. Braude, A. S. et al. No detection of SO_2, H_2S, or OCS in the atmosphere of Mars from the first two Martian years of observations from TGO/ACS. *Astron. Astrophys.* **658**, A86 (2022).
62. Christensen, P. R. et al. Morphology and composition of the surface of Mars: Mars Odyssey THEMIS results. *Science* **300**, 2056–2061 (2003).

[1]Space Research and Planetary Sciences, Physics Institute, University of Bern, Bern, Switzerland. [2]Department of Earth, Environmental and Planetary Sciences, Brown University, Providence, RI, USA. [3]The Royal Observatory of Belgium (ROB-ORB), Brussels, Belgium. [4]Archaeology, Environmental Changes & Geo-chemistry (AMGC) Research Unit, Vrije Universiteit Brussel, Brussels, Belgium. [5]Institute of Astronomy, KU Leuven, Leuven, Belgium. [6]Institute of Planetary Research, German Aerospace Center (DLR), Berlin, Germany. [7]Center for Space and Habitability, University of Bern, Bern, Switzerland. [8]INAF-Osservatorio Astronomico di Padova, Padova, Italy. [9]Istituto di Astrofisica e Planetologia Spaziali, IAPS-INAF, Rome, Italy. [10]GEOPS, Université Paris-Saclay, CNRS, Orsay, France. [11]Institut Universitaire de France, Paris, France. [12]Royal Belgian Institute for Space Aeronomy (BIRA-IASB), Brussels, Belgium. [13]Lunar and Planetary Laboratory, University of Arizona, Tuscon, AZ, USA. [14]Institute for Earth and Space Exploration, Department of Earth Sciences, Western University, London, Ontario, Canada. [15]Space and Planetary Science Center and Department of Earth Sciences, Khalifa University, Abu Dhabi, United Arab Emirates. [16]School of Physical Sciences, The Open University, Milton Keynes, UK. [17]Instituto de Astrofísica de Andalucia, Granada, Spain. ✉e-mail: adomas_valantinas@brown.edu

Methods

CaSSIS frost observations

We surveyed ~4,200 CaSSIS images (acquired up to 2022 February 05) with illumination geometries of 50–90° incidence within dusty, low thermal inertia (<100 TIU) regions (60° N–30° S). Only images that include the latest CaSSIS radiometric and absolute calibration were used in this study[43,63,64].

The images used in this study consisted of early (6:00–9:00 LST) and late (15:00–18:00 LST) times. Analysis and comparison in these two local time regimes may help the distinction between early-morning and late-afternoon phenomena. During the survey, it was noticed that most CaSSIS images acquired at extremely high solar incidence angles of 85–90° contain colour and calibration artefacts due to the decrease in SNR and/or an increase in aerosol contribution from the atmosphere[63]. Consequently, the images with colour artefacts were labelled as ambiguous and were not used for further analysis.

Frost detections relied on the use of CaSSIS NPB (near infrared (NIR) = 940, panchromatic (PAN) = 670, blue (BLU) = 497 nm) and synthetic RGB (red–green–blue; PAN and BLU only) products. These filter configurations allow a convenient separation between frosty and frost-free terrains. In CaSSIS colour products, frosty areas appear bluish, and/or whitish, and sometimes are bright only in the BLU filter (relative to frost-free areas; also see Supplementary Figs. 9 and 10). In support, we observe bluish frost deposits in HRSC colour images shown in Fig. 1b and Extended Data Fig. 1 (composites of blue (440 nm), green (530 nm) and red (750 nm) channels).

As shown by previous studies[21,65] deposits are usually correlated with topography (prefer poleward-sloping terrains). Therefore, if both conditions were met (colour and topographic correlation), it was considered a strong indication of surface frost. As a final procedure, each of these candidate detections was then analysed using a spectral profile tool in the Environment for Visualizing Images software. This procedure extracts the pixel irradiance over flux (*I/F*) values between two manually selected points crossing the potentially frosted region in each filter. The profiles were then normalized by a mean *I/F* of a nearby frost-free, relatively flat region of interest (ROI), a well-established method to cancel out some of the atmospheric and topographic effects[49,66–70]. If the frost deposits were brighter in the BLU filter than the surrounding frost-free terrains by at least 3% (within CaSSIS absolute uncertainty[43]), then such images were flagged as potential frost detections. This survey yielded many frosty sites (not shown here) at latitudes ~40° N and ~30° S. However, because these latitude bands are dominated by known seasonal frost deposits[21,23,65] and we do not have a robust method to distinguish between seasonal and diurnal frost, we further narrowed our filtering criteria. The final frost detections analysed here were restricted to equatorial ~20° N to ~10° S latitudes (outside of the seasonal mid-latitude regions). In this work, only equatorial sites that included visible evidence of frost are considered.

The spectral profile shown in Fig. 2e was computed by dividing each pixel along the profile by an average pixel value extracted from an ROI in Extended Data Fig. 5d. The ROI (>100 pixels in size) was selected on a frost-free and relatively flat terrain as suggested by the low slope values in the CaSSIS digital elevation model of this site. CaSSIS digital elevation models were produced by a pipeline developed at the Astronomical Observatory of Padova, National Institute for Astrophysics[71,72].

NOMAD-LNO spectral processing

The NOMAD instrument is a suite of three high-resolution spectrometers also on board TGO, offering nadir infrared observations through its LNO channel[37,73]. This channel covers the 2.2–3.8 μm spectral range where several spectral features of ice are distributed over different wavelengths. Nevertheless, the NOMAD-LNO spectrometer has the particularity of not observing the entire spectral range at once. The data are acquired through small spectral windows, representing specific diffraction orders of the diffraction grating. Each LNO observation can select a maximum number of 6 diffraction orders every 15 seconds to ensure the best possible SNR[74–76]. The LNO footprint (instantaneous field of view) is 17.5 km × 0.5 km (ref. 75), which provides enough spatial scale to resolve the caldera of Olympus Mons. In this work, we use spectrally and radiometrically calibrated LNO data converted into a reflectance factor. The 2.7 μm ice band is the strongest in the LNO spectral range, resulting from both CO_2 and H_2O ice absorption. Although the use of this band is not suitable for quantifying the amount of ice (easily saturated), it is effective for detecting homogeneous deposits (both CO_2 and H_2O ice), as demonstrated with the ice index value[77]. This spectral parameter uses two diffraction orders. It is based on the combination of high reflectivity at continuum wavelengths with a more pronounced absorption in the 2.7 μm band. Initially defined as the spectral ratio between the reflectance factors of order 190 (continuum part, 2.32–2.34 μm) and 169 (short wavelengths shoulder of the 2.7 μm band, 2.61–2.63 μm) (ref. 77), we adjust the ice index by considering the available orders of the joint CaSSIS–NOMAD observations, that is, orders 190 and 168 (2.64–2.65 μm).

In nadir mode, the variability in the reflectance factors is caused mainly by the surface albedo variations resulting from the different absorption of the Martian surface mineralogy[78–80]. To remove spatial albedo variations over the explored Martian surface, we normalize the LNO reflectance factors to the Martian albedo. The adjusted ice index (II) can thus be defined as:

$$\mathrm{II} = \frac{R_{2.33}}{\mathrm{OMEGA}_{2.32}} \div \frac{R_{2.63}}{\mathrm{OMEGA}_{2.62}}$$

where R_i is the LNO reflectance factor value averaged around the central wavelength i of the LNO spectrum, fitted by a third-degree polynomial to mitigate the spectral oscillations resulting from the instrumental characteristics of the LNO channel, which become significant on the edges of each order (Supplementary Figs. 1 and 2). OMEGA_i is the OMEGA albedo map[80] based on reflectance spectra in the near infrared as NOMAD-LNO R_i. Two OMEGA albedo maps are used in this work: one defined at 2.32 μm for order 190 and the other defined at 2.62 μm for order 168. Studies have shown that this spectral parameter identifies spatially extensive and abundant ice deposits when the index values are three sigma higher than their average value over ice-free mid-latitude terrain[77,81].

Mars GCM modelling

We perform the Martian GCM simulation for the entire MY 36 using the MarsWRF model, which is the Mars adaptation of the general-purpose planetary atmosphere model, planetWRF[47]. Here the GCM set-up is based on a previous study[46] examining the Martian planetary boundary and dust–turbulence interaction over a decade, from MY 24 to MY 34, which hosted three global dust storms. The reference model set-up[46] was validated against NASA's Mars Climate Sounder (MCS) observations on board the Mars Reconnaissance Orbiter, radio occultation observations from ESA's Mars Express orbiter, as well as the in situ observations from NASA's Mars Science Laboratory Curiosity rover. This model set-up consists of a semi-interactive two-moment dust transport model[46] within the MarsWRF framework, in a way that the dust is lifted, mixed by model winds and sedimented, as guided by observed maps of column-integrated dust optical thickness[82,83]. Via this method, model processes govern the vertical dust distribution and related dust radiative heating, yet the horizontal dust distribution is guided to match the orbiter observations. In this model, the horizontal dust distribution is constrained to follow observations. In this model, the two-stream correlated *k*-distribution scheme is used for the short-wave and long-wave radiative transfer[84]. We use a Mars-specific boundary-layer turbulence parameterization scheme, which allows us to obtain the surface–atmosphere exchange coefficients[85] Surface properties of the MarsWRF model, such as the topography, albedo, emissivity and thermal inertia, are acquired from the datasets of the

Mars Orbiter Laser Altimeter[2] and Thermal Emission Spectrometer (TES[78]) observations, where the details are presented in another study[47]. Here we increased the horizontal model grid spacing of the GCM from 5° × 5° to 2.5° × 2.5° (ref. 46), enabling better spatial coverage to provide more realistic boundary and initial conditions to our mesoscale simulations. We used 52 vertical sigma layers extending up to the model top of 100 km. The predicted surface temperatures are shown in Table 1.

Our modelling methodology is based on a previous study by MarsWRF[85,86]. Mesoscale simulations for Fig. 5 and Extended Data Fig. 7 were forced with initial and boundary conditions acquired by GCM simulations corresponding to the same seasonal conditions of CaSSIS observations shown in Figs. 1 and 2. The plots we present in terms of winds, pressure and temperature correspond to the local hours of observations. We nested three mesoscale domains in our GCM domain (see Supplementary Fig. 12 for details). Mesoscale domains use prescribed boundary conditions, derived either from GCM predictions (as in the case of d2) or from another mesoscale domain (d3 and d4). The GCM grid has a horizontal resolution of approximately 150 km. We progressively increased the horizontal resolution with a factor of three for our nested mesoscale domains. Our innermost domain, d4, has a horizontal resolution of 5.47 km. To assess the accuracy of our mesoscale predictions, we compared MarsWRF surface temperature predictions with the surface temperature observations by MCS and TES available for Olympus Mons and Arsia Mons regions at around 3:00 LST (Supplementary Fig. 13). We considered a sufficient Ls range of MCS and TES observations (Ls 310–360 for Olympus Mons and Ls 75–100 for Arsia Mons) to provide a sufficient set of observations to acquire a temperature map to be compared with MarsWRF simulations. These observations range from 1:00 LST to 4:00 LST, and MarsWRF estimations at the corresponding local times are compared for validation. The modelled surface temperatures for Olympus Mons caldera are within 10 K of the observations and within a few degrees Kelvin for Arsia Mons. It is important to note that these predictions carry uncertainties, particularly in regions with complex topography such as the Tharsis volcanoes.

Surface frost thickness and mass estimations

The MarsWRF GCM incorporates the phase transition and transport mechanisms of water vapour and ice, facilitating a parameterization of the Martian hydrological cycle that aligns with the methodologies outlined by previous studies[87]. This parameterization enables the model to approximate the surface frost layer thickness to about 1 µm at the locations in our study. However, it is important to acknowledge the inherent uncertainties associated with such estimations, particularly due to the limitations of physical parameterizations within Martian atmospheric models. These uncertainties are most pronounced in the prediction of atmospheric variables in regions lacking empirical observational data, such as the deposition rates of atmospheric volatiles.

In a recent experimental investigation, one study[52] systematically evaluated the interaction between water frost deposition and the optical properties of a Martian soil simulant, specifically Mars Global Simulant (MGS-1[88]). The experimental design involved the controlled deposition of water frost on the surface of the simulant, followed by precise measurements of both the spectral reflectance and the thickness of the frost layer. The findings indicate that a frost layer thickness ranging from approximately 10 to 20 µm is required to significantly attenuate the characteristic red slope of the spectral reflectance, aligning with the observed morning frost brightening in the blue wavelengths by approximately 10–20% as detected by the CaSSIS instrument. Furthermore, the study demonstrates that a relatively thin frost layer of about 100 µm is sufficient to flatten the visible spectrum, effectively neutralizing the spectral features.

Radiative transfer models[50,51] can provide an additional constraint on the frost thickness estimation via the minimum optical depth (τ) necessary for frost visibility at CaSSIS visible and LNO near-infrared wavelengths. For example, with a τ of 10^{-2}, we anticipate a minimal impact on albedo, less than 0.1 at CaSSIS visible wavelengths and negligible at LNO near-infrared wavelengths, given the single-scattering co-albedo is around 10^{-6} for visible light and less than 10^{-1} at 2.6 µm. However, LNO observations indicate a discernible albedo reduction at near-infrared wavelengths, suggesting a higher optical depth than 10^{-2}. This implies that the frost's grain radius and/or thickness must exceed 5 µm and 1 µm, respectively. If the grain radius is about 1 µm, then the frost layer's thickness could be significantly greater, approximately 100 µm.

To conduct a preliminary quantification of the frost mass, we assumed a uniform frost layer thickness across all identified frost-covered regions, as observed by CaSSIS. The geographical extent of the frost coverage was approximated to the combined surface areas of the calderas of Martian volcanoes such as Arsia Mons, Olympus Mons, Ascraeus Mons and Ceraunius Tholus. By integrating the uniform frost thickness with the delineated area and adopting the density value for pure ice, we derived an initial estimate of the total frost mass. This approach provides a rudimentary yet insightful approximation of the frost mass, acknowledging the broad-scale estimative nature of this calculation.

Boulder size measurements

To investigate a potential effect of the diurnal frost cycle on the overall geomorphology and landscape evolution, we studied the shape of mass-wasted boulders across six sites of interest. Here we compare the sizes of boulders on volcanoes with frost as determined by CaSSIS (two sites in Olympus Mons and one in Arsia Mons) and on volcanoes where frost has not been detected (Tharsis Mons, Jovis Tholus and Ulysses Tholus). Because frost accumulates preferentially on poleward-facing slopes on Mars[29], here we focused only on north-facing and south-facing slopes. This might reveal whether there are considerable differences in boulder sizes due to frost weathering[89].

We used eight map-projected High Resolution Imaging Science Experiment (HiRISE)[90] images in Geographic Information System (QGIS) to determine the three principal dimensions of each identified boulder. The first dimension is defined as the longest distance between two points on the boulder as visible from orbit. Similarly, the second dimension is defined as the diameter of the boulder orthogonal to the first dimension. Last, the third dimension is defined as the height of the boulder as estimated using shadow length and solar incidence angle. In total, we identified and measured 63 boulders across the six sites. All derived measurements were plotted on ternary diagrams[91] using the Tri-Plot software[92]. These diagrams relate the three principal dimensions of each boulder, visualizing its overall shape as well as similarities and differences within and across the studied sites.

Data availability

CaSSIS data can be found on the University of Bern repository (https://observations.cassis.unibe.ch/) and the ESA's Planetary Science Archive (https://archives.esac.esa.int/psa). NOMAD-LNO observations are also found on the ESA's Planetary Science Archive.

Code availability

The PlanetWRF model for Martian GCM and mesoscale simulations is accessible by request at https://planetwrf.com/.

References

63. Pommerol, A. et al. In-flight radiometric calibration of the ExoMars TGO Colour and Stereo Surface Imaging System. *Planet. Space Sci.* **223**, 105580 (2022).
64. Almeida, M. et al. Targeting and image acquisition of Martian surface features with TGO/CaSSIS. *Planet. Space Sci.* **231**, 105697 (2023).
65. Vincendon, M., Forget, F. & Mustard, J. Water ice at low to midlatitudes on Mars. *J. Geophys. Res. Planets* **115**, E10001 (2010).

66. Daubar, I. J. et al. Changes in blast zone albedo patterns around new Martian impact craters. *Icarus* **267**, 86–105 (2016).
67. Schaefer, E. I., McEwen, A. S. & Sutton, S. S. A case study of recurring slope lineae (RSL) at Tivat crater: implications for RSL origins. *Icarus* **317**, 621–648 (2019).
68. Munaretto, G. et al. Implications for the origin and evolution of Martian recurring slope lineae at Hale crater from CaSSIS observations. *Planet. Space Sci.* **187**, 104947 (2020).
69. Munaretto, G. et al. Topographic correction of HiRISE and CaSSIS images: validation and application to color observations of Martian albedo features. *Planet. Space Sci.* **200**, 105198 (2021).
70. Munaretto, G. et al. Multiband photometry of Martian recurring slope lineae (RSL) and dust-removed features at Horowitz crater, Mars from TGO/CaSSIS color observations. *Planet. Space Sci.* **214**, 105443 (2022).
71. Simioni, E. et al. 3DPD: a photogrammetric pipeline for a PUSH frame stereo cameras. *Planet. Space Sci.* **198**, 105165 (2021).
72. Re, C. et al. CaSSIS-based stereo products for Mars after three years in orbit. *Planet. Space Sci.* **219**, 105515 (2022).
73. Neefs, E. et al. NOMAD spectrometer on the ExoMars Trace Gas Orbiter mission: part 1—design, manufacturing and testing of the infrared channels. *Appl. Opt.* **54**, 8494–8520 (2015).
74. Thomas, I. R. et al. Optical and radiometric models of the NOMAD instrument part II: the infrared channels—SO and LNO. *Opt. Express* **24**, 3790–3805 (2016).
75. Thomas, I. R. et al. Calibration of NOMAD on ESA's ExoMars Trace Gas Orbiter: part 2—the limb, nadir and occultation (LNO) channel. *Planet. Space Sci.* **218**, 105410 (2022).
76. Liuzzi, G. et al. Methane on Mars: new insights into the sensitivity of CH_4 with the NOMAD/ExoMars spectrometer through its first in-flight calibration. *Icarus* **321**, 671–690 (2019).
77. Oliva, F. et al. Martian CO_2 ice observation at high spectral resolution with ExoMars/TGO NOMAD. *J. Geophys. Res. Planets* **127**, e2021JE007083 (2022).
78. Christensen, P. R. et al. Mars Global Surveyor Thermal Emission Spectrometer experiment: investigation description and surface science results. *J. Geophys. Res. Planets* **106**, 23823–23871 (2001).
79. Viviano-Beck, C. E. et al. Revised CRISM spectral parameters and summary products based on the currently detected mineral diversity on Mars. *J. Geophys. Res. Planets* **119**, 1403–1431 (2014).
80. Riu, L. et al. The M3 project: 1—a global hyperspectral image-cube of the Martian surface. *Icarus* **319**, 281–292 (2019).
81. Ruiz Lozano, L. et al. Evaluation of the capability of ExoMars-TGO NOMAD infrared nadir channel for water ice clouds detection on Mars. *Remote Sens.* https://doi.org/10.3390/rs14174143 (2022).
82. Montabone, L. et al. Eight-year climatology of dust optical depth on Mars. *Icarus* **251**, 65–95 (2015).
83. Montabone, L. et al. Martian year 34 column dust climatology from Mars climate sounder observations: reconstructed maps and model simulations. *J. Geophys. Res. Planets* **125**, e2019JE006111 (2020).
84. Mischna, M. A., Lee, C. & Richardson, M. Development of a fast, accurate radiative transfer model for the Martian atmosphere, past and present. *J. Geophys. Res. Planets* **117**, E10009 (2012).
85. Temel, O. et al. Large eddy simulations of the Martian convective boundary layer: towards developing a new planetary boundary layer scheme. *Atmos. Res.* **250**, 105381 (2021).
86. Temel, O. et al. Strong seasonal and regional variations in the evaporation rate of liquid water on Mars. *J. Geophys. Res. Planets* **126**, e2021JE006867 (2021).
87. Richardson, M. I. & Wilson, R. J. Investigation of the nature and stability of the Martian seasonal water cycle with a general circulation model. *J. Geophys. Res. Planets* **107**, 7–28 (2002).
88. Cannon, K. M., Britt, D. T., Smith, T. M., Fritsche, R. F. & Batcheldor, D. Mars global simulant MGS-1: a Rocknest-based open standard for basaltic Martian regolith simulants. *Icarus* **317**, 470–478 (2019).
89. Hales, T. C. & Roering, J. J. Climatic controls on frost cracking and implications for the evolution of bedrock landscapes. *J. Geophys. Res. Earth Surf.* **112**, F02033 (2007).
90. McEwen, A. S. et al. Mars Reconnaissance Orbiter's High Resolution Imaging Science Experiment (HiRISE). *J. Geophys. Res.* **112**, E05S02 (2007).
91. Sneed, E. D. & Folk, R. L. Pebbles in the lower Colorado River, Texas: a study in particle morphogenesis. *J. Geol.* **66**, 114–150 (1958).
92. Graham, D. J. & Midgley, N. G. Graphical representation of particle shape using triangular diagrams: an Excel spreadsheet method. *Earth Surf. Process. Landf.* **25**, 1473–1477 (2000).

Acknowledgements

CaSSIS is a project of the University of Bern and funded through the Swiss Space Office via ESA's PRODEX programme. The instrument hardware development was also supported by the Italian Space Agency (ASI) (ASI-INAF agreement no. 2020-17-HH.0), INAF/Astronomical Observatory of Padova and the Space Research Center (CBK) in Warsaw. Support from SGF (Budapest), the University of Arizona (Lunar and Planetary Lab.) and NASA is also gratefully acknowledged. Operations support from the UK Space Agency under grant ST/R003025/1 is also acknowledged. The NOMAD experiment is led by the Royal Belgian Institute for Space Aeronomy (IASB-BIRA), assisted by Co-PI teams from Spain (IAA-CSIC), Italy (INAF-IAPS) and the United Kingdom (Open University). This project acknowledges funding by the Belgian Science Policy Office (BELSPO), with the financial and contractual coordination by the ESA Prodex Office (PEA 4000103401, 4000121493) and Italian Space Agency through grant 2018-2-HH.0. Operations and science support from the UK Space Agency under grants ST/X006549/1, ST/Y000234/1, ST/V005332/1 and ST/V002295/1 is also acknowledged. This research is financially supported by the Research Foundation-Flanders (FWO) with grant 12AM624N to C.B.S., and grant 12ZZL23N to O.T. J.J.L.-M. acknowledges financial support from the Severo Ochoa grant CEX2021-001131-S funded by MCIN/AEI/ 10.13039/501100011033 and by Spanish MICIIN through Plan Nacional and European funds. F.S. acknowledges support from the Institut National des Sciences de l'Univers (INSU), the Centre National de la Recherche Scientifique (CNRS) and Centre National d'Etudes Spatiales (CNES) through the Programme National de Planétologie. MRELM acknowledges funding from the KU internal grant (8474000336-KU-SPSC).

Author contributions

A.V. led conceptualization, CaSSIS data collection and analysis, and writing. N.T. and A.P. led conceptualization, design and production of the CaSSIS instrument and its operation. O.T., C.B.S. and O.K. performed mesoscale and global circulation model simulations with MarsWRF, did post-processing of the modelling results and compared model predictions with MCS and TES observations, which were analysed by O.T. and O.K. L.R.L. and F.O. performed NOMAD spectral analysis. G.M. and M.P. performed CaSSIS clustering analysis and photometry. V.T.B. processed HiRISE data, performed boulder size measurements and analyzed boulder shapes. L.R.L., V.T.B., G.M., M.P., F.S., A.P., A.S.M., M.R.E.-M., V.G.R., N.T. and I.T. contributed to writing. F.G.C., A.P., N.T., G.B. and E.D. contributed to discussions and assisted with data interpretation. C.R., G.B. and I.T. contributed to data processing. A.C.V., J.J.L.-M., F.D. and M.R.P. contributed to the design and production of the NOMAD instrument and its operation. D.T., E.H., M.R., M.A., I.T. and B.R. participated in instrument operations and planning of the observations. N.T. and G.C. acquired funds for the development of the CaSSIS instrument and the generation of DEMs. A.C.V. and F.D. acquired funds for the development of the NOMAD instrument.

Funding

Open access funding provided by University of Bern.

Competing interests
The authors declare no competing interests.

Additional information
Extended data is available for this paper at https://doi.org/10.1038/s41561-024-01457-7.

Supplementary information The online version contains supplementary material available at https://doi.org/10.1038/s41561-024-01457-7.

Correspondence and requests for materials should be addressed to A. Valantinas.

Peer review information *Nature Geoscience* thanks Daniel Viudez-Moreiras and Aditya Khuller for their contribution to the peer review of this work. Primary Handling Editor: Tamara Goldin, in collaboration with the *Nature Geoscience* team.

https://doi.org/10.1038/s41561-024-01457-7

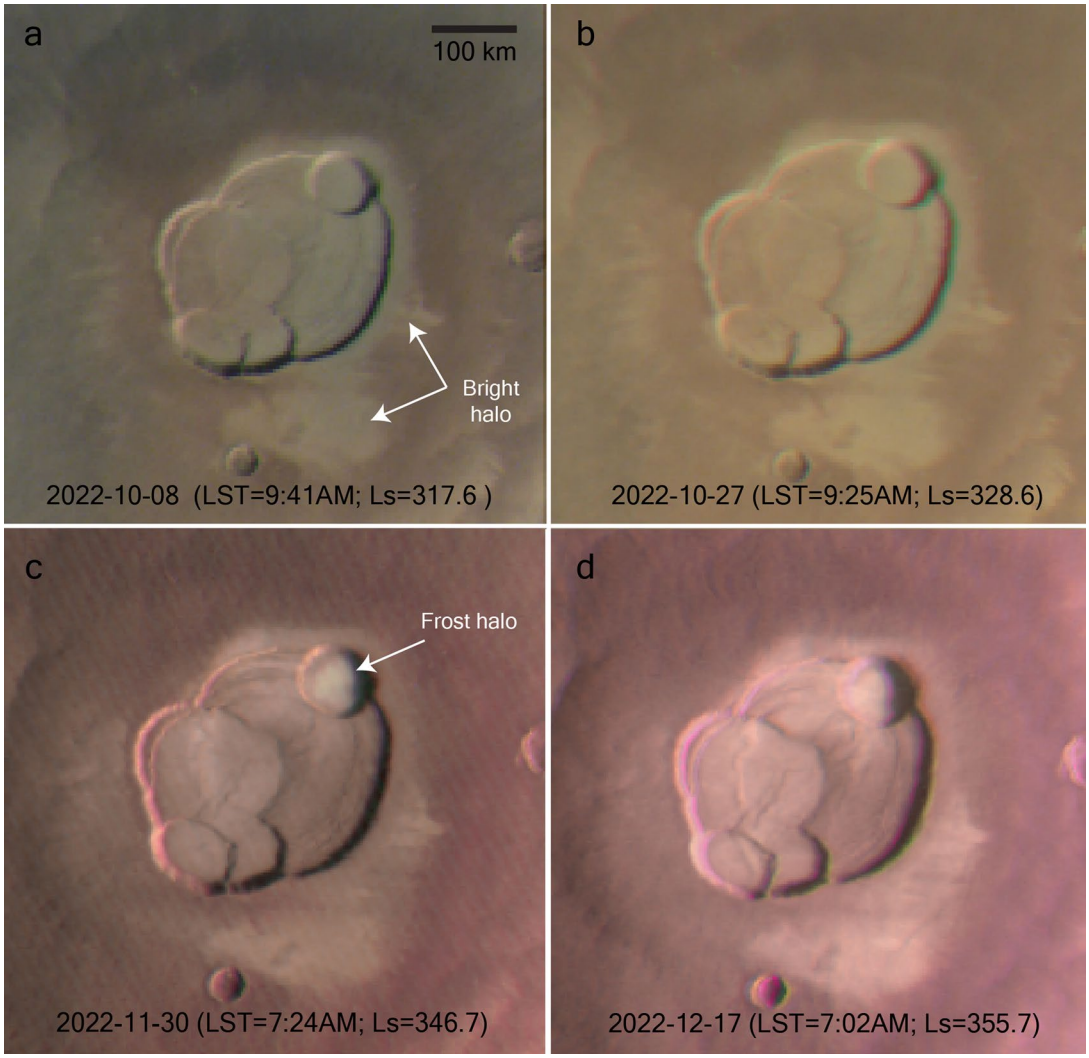

Extended Data Fig. 1 | Diurnal variations of frost halo on Olympus Mons. HRSC images of Olympus Mons (lat = 18.2°N, lon = −133.2°E) acquired at different local times in MY 36. (**a, b**) Late morning images showing no evidence of frost on the bright halo deposit surrounding the volcano caldera. (**c, d**) Early morning images revealing the presence of frost on the bright halo deposit. The bright halo deposit is likely composed of fine-grained dust with low thermal conductivity, which facilitates frost formation. North is up in all panels. HRSC image IDs: hn705_0000 (a), hn772_0000 (**b**), hn889_0000 (**c**), hn948_0000 (**d**). Credit: ESA/DLR/FU Berlin.

https://doi.org/10.1038/s41561-024-01457-7

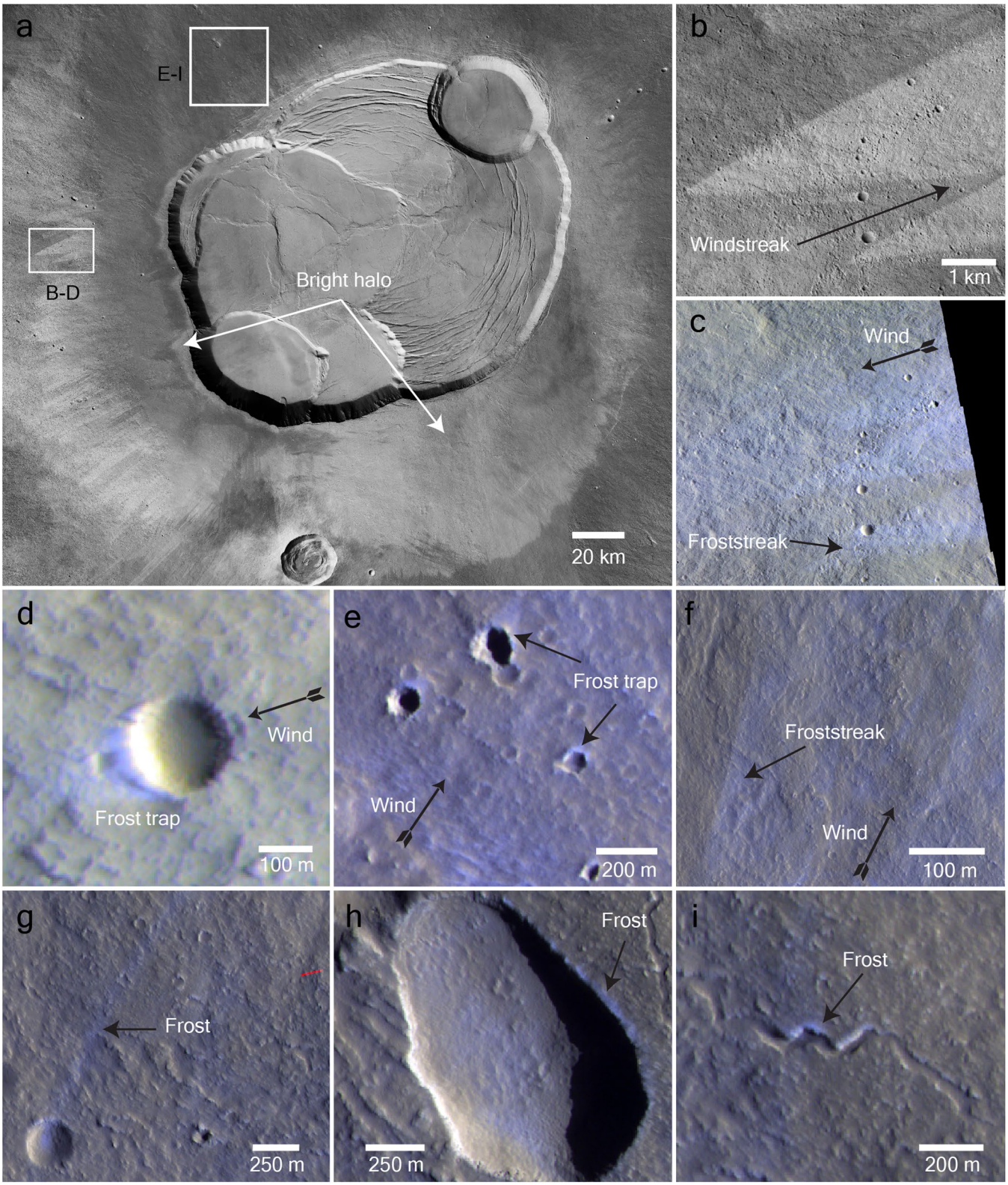

Extended Data Fig. 2 | Irregular frost distribution on the outskirts of Olympus Mons caldera. (**a**) Bright halo visible in the CTX global mosaic (Dickson et al., 2018). The bright halo deposit is also visible in HRSC non-detections in Extended Data Fig. 1. (**b**) Dark windstreak and triangular bright unremoved dust deposits seen in CTX. (**c**) CaSSIS morning observation of froststreaks (lat/lon = 18.28°N, −134.24°E) that correlate with bright dust deposits seen in CTX. (**d, e**) Frost deposits leeward of small craters (lat/lon: 18.27°N, −134.24°E and 18.83°N, −133.65°E respectively). (**f, g**) Froststreaks that are parallel to local winds (lat/lon: 18.90°N, −133.65°E and 18.9°N −133.74°E respectively). (**h, i**) Small frost deposits on the rim of a collapse pit (lat/lon: 18.95°N, −133.69°E) and on the levee of a lava channel (lat/lon: 19.00°N, −133.71°E). North is up in all panels. CaSSIS IDs: MY37_023825_162_0 (LST =7:13AM; Ls = 42.84; c,d) and MY36_015229_160_0 (LST = 6:57AM; Ls = 35.24 ; e-i). Credit: **a**,**b**, NASA/JPL/MSSS/The Murray Lab; **c**–**l**, ESA/TGO/CaSSIS under a Creative Commons license CC-BY-SA 3.0 IGO.

https://doi.org/10.1038/s41561-024-01457-7

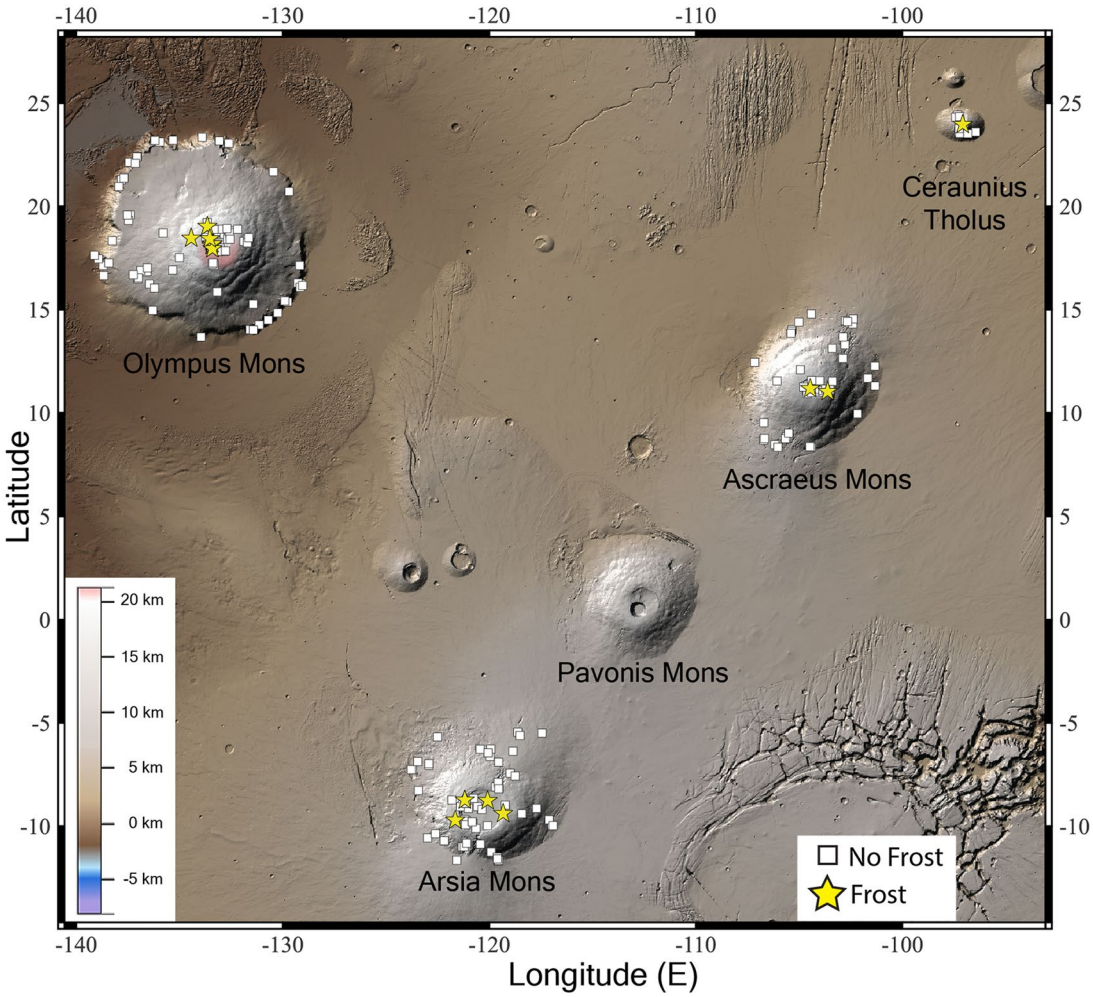

Extended Data Fig. 3 | CaSSIS frost detections in the Tharsis volcanic region. Frost was detected only on and around the calderas of the three largest volcanoes such as Olympus, Arsia and Ascraeus Montes, but also on the smaller Ceraunius Tholus volcano. Frost has not been observed yet on Pavonis Mons and other Tharsis volcanoes. The basemap is the color hillshade MOLA data at 64 pixels per degree resolution. Credit: NASA/JPL/GSFC.

https://doi.org/10.1038/s41561-024-01457-7

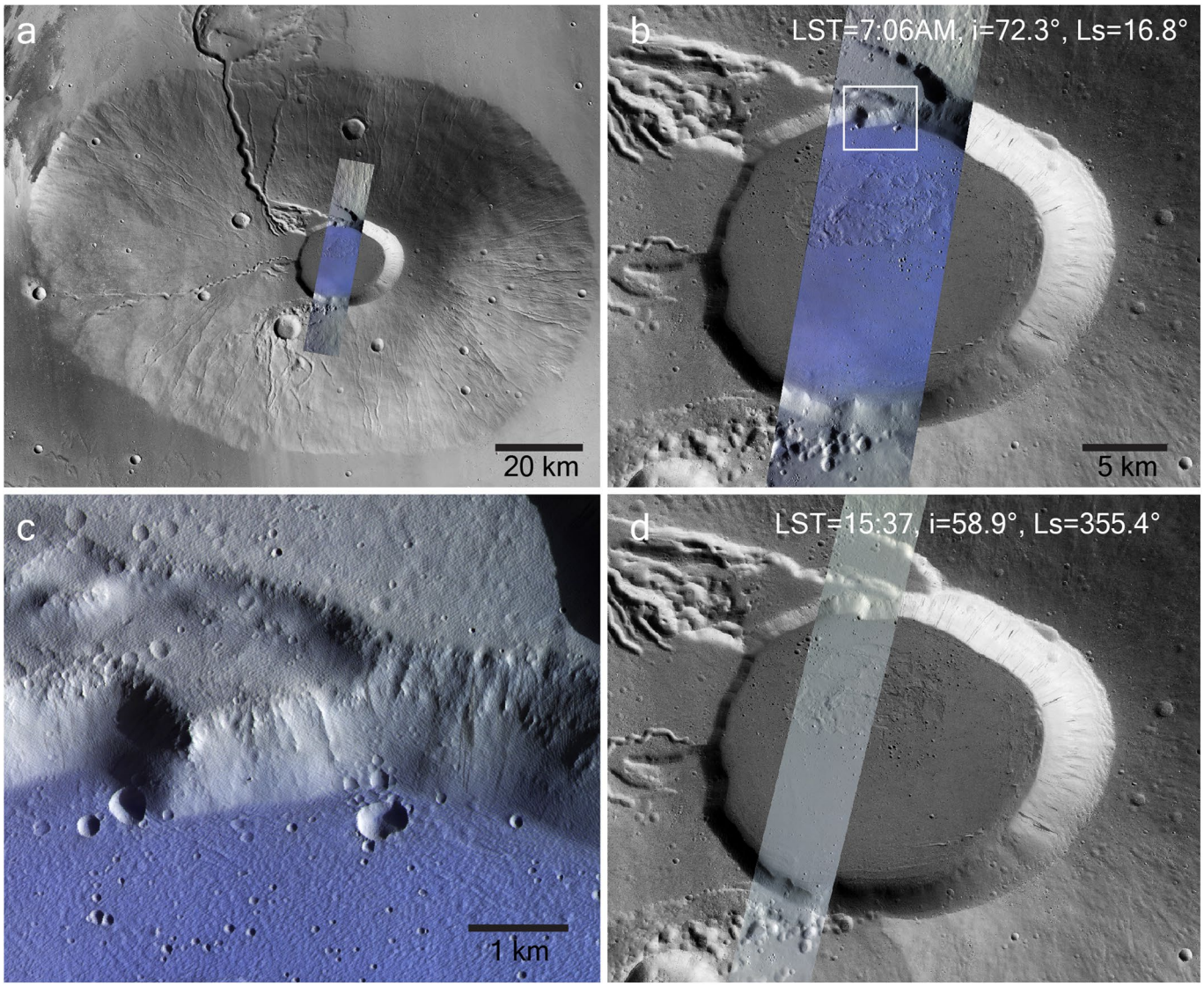

Extended Data Fig. 4 | Frost on the caldera floor of Ceraunius Tholus volcano. (**a**) Wide angle view of Ceraunius Tholus (lat = 24.0°N, lon = −97.1°E) with CaSSIS early morning observation overlain on the CTX mosaic. (**b**) Zoomed in view of (a). White rectangle marks the close up in (c). (**c**) Ubiquitous frost coverage on the caldera floor and the apparent absence of frost on the caldera rim. (**d**) CaSSIS color NPB image of the Ceraunius Tholus caldera acquired at a different local time featuring no frost. Both CaSSIS images in (b) and (d) are acquired at similar incidence (and phase) angles, which suggests that photometric effects are not the cause of surface blueing. North is up in all panels. CaSSIS image IDs in order: MY37_023134_024_3_NPB (**a**–**c**) and MY36_022599_024_0_NPB (**d**). **a**,**b**,**d**, NASA/JPL/MSSS/The Murray Lab; **a**, **b**, **c**, **d**, ESA/TGO/CaSSIS under a Creative Commons license CC-BY-SA 3.0 IGO.

https://doi.org/10.1038/s41561-024-01457-7

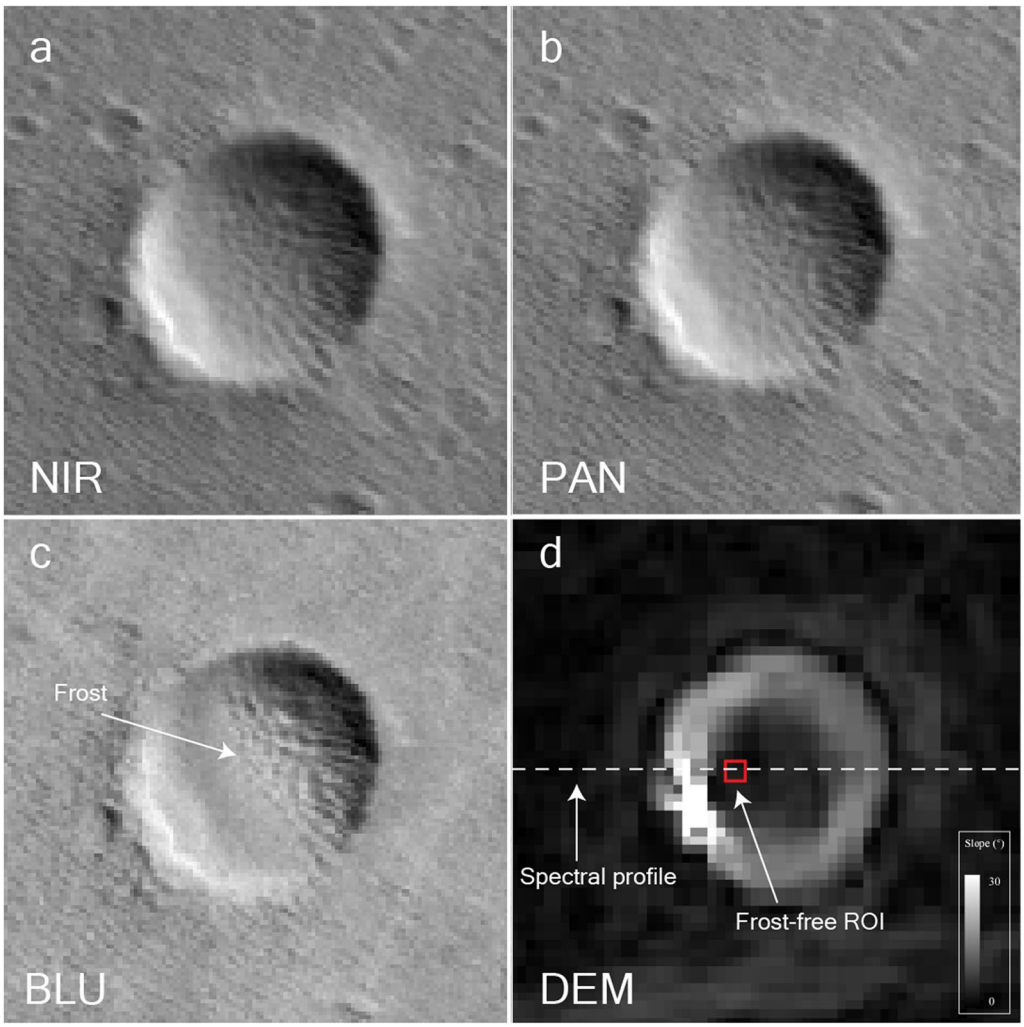

Extended Data Fig. 5 | Greyscale CaSSIS filter images of a small crater presented in Fig. 2. (**a**–**c**) Three individual filters: NIR (860–1100 nm), PAN (550–800 nm) and BLU (390–570 nm). (**d**) CaSSIS DEM of the same scene with the location of the spectral profile and the frost-free ROI used in the reflectance ratio (Methods) overlaid. The frost deposits are brighter and visible in the CaSSIS BLU filter. North is up in all panels. CaSSIS ID: MY35_008465_192_0 (**a**–**c**) and DEM ID: CAS-DTM-MY36_020366_190_1-OPD-03–01 (**d**). Credit: ESA/TGO/CaSSIS under a Creative Commons license CC-BY-SA 3.0 IGO.

https://doi.org/10.1038/s41561-024-01457-7

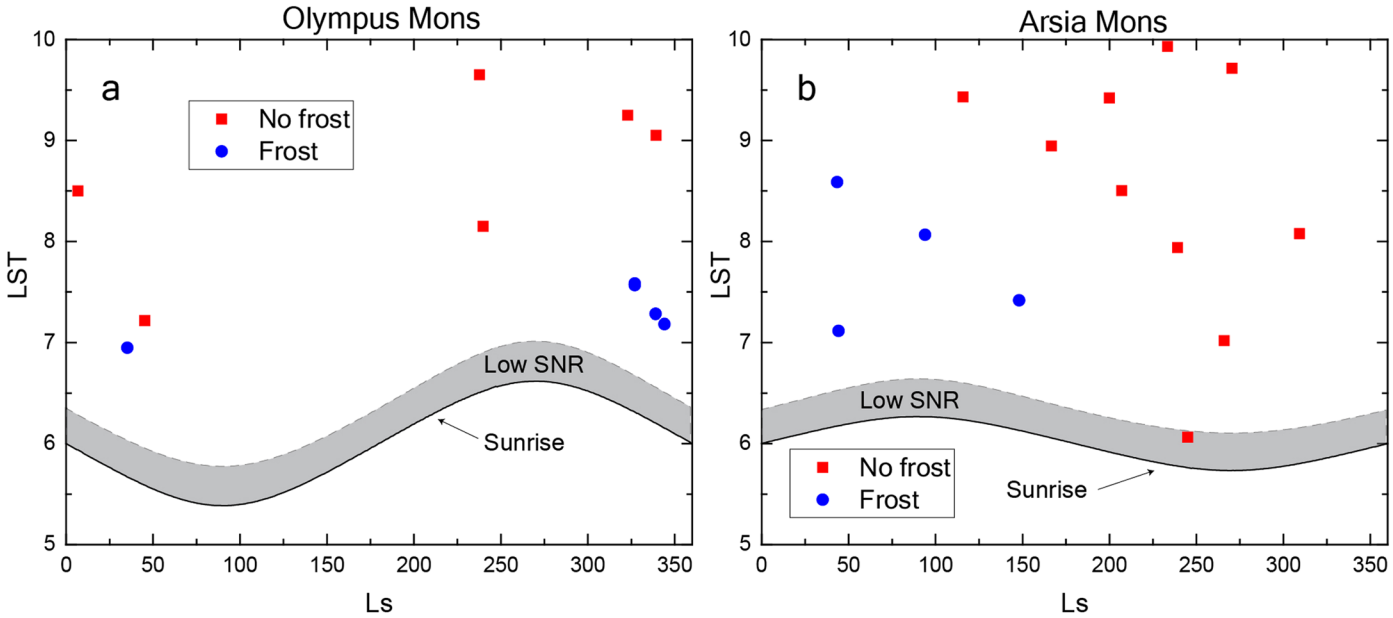

Extended Data Fig. 6 | Seasonal and local time coverage of CaSSIS early morning observations of Olympus Mons and Arsia Mons. CaSSIS image coverage over Olympus Mons (**a**) and Arsia Mons (**b**). Based on these observations frost is not detected during late morning hours in Olympus Mons and around southern summer solstice (Ls ~270°) in Arsia Mons. The shaded grey region shows the CaSSIS observational bias (from 90 – 85° solar incidence) due to the low signal-to-noise ratio. Most observations were discarded in this region due to spectral ambiguity. The black lines mark the local sunrise time.

https://doi.org/10.1038/s41561-024-01457-7

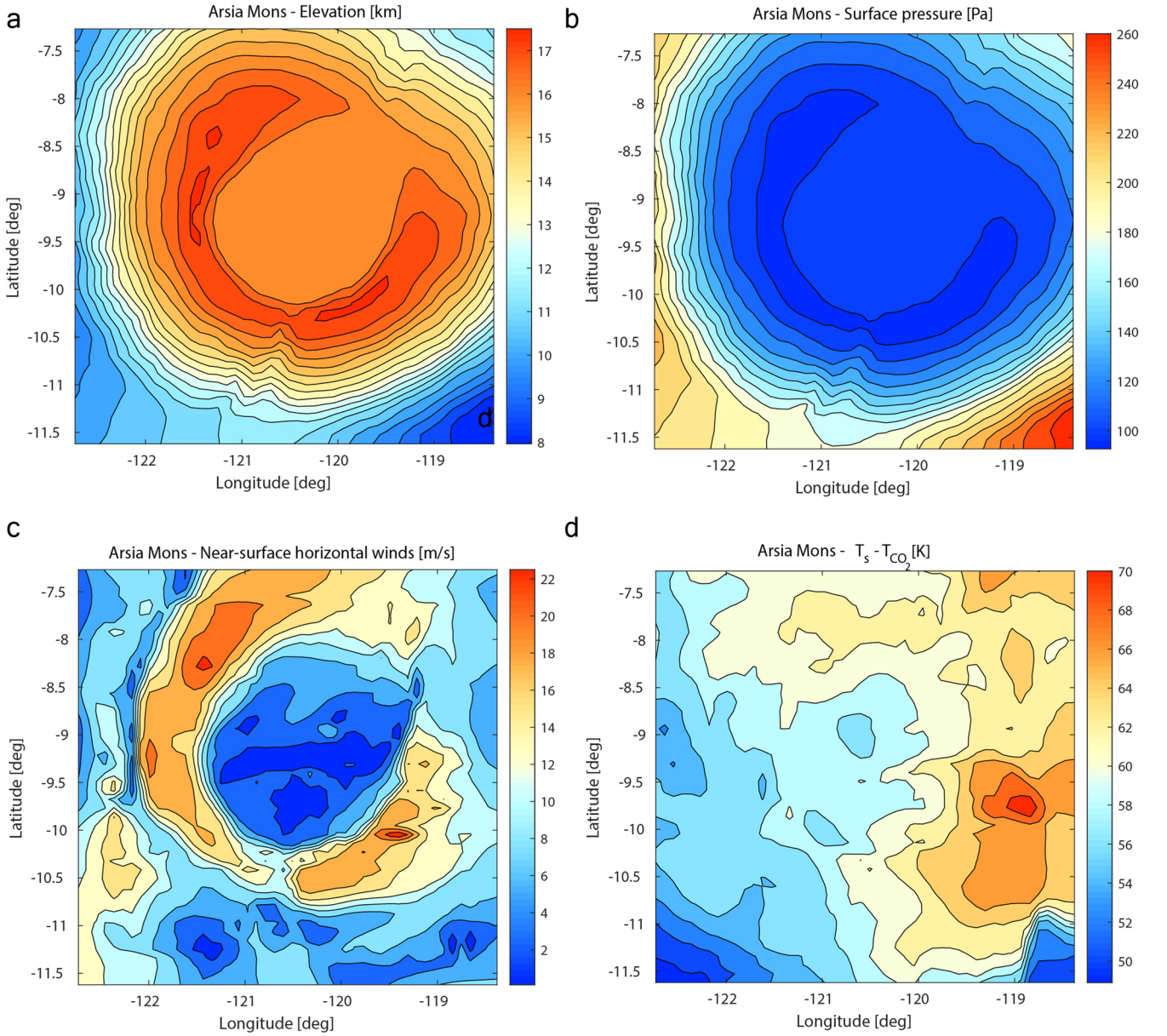

Extended Data Fig. 7 | Microclimatic conditions simulated over Arsia Mons. This figure illustrates the impact of Arsia Mons' topography on localized atmospheric conditions (at 8AM, Ls = 90°, Fig. 2a), depicted through (**a**) elevation gradients, (**b**) surface atmospheric pressure, (**c**) near-surface horizontal wind patterns, and (**d**) the temperature differential between the Martian surface and the local CO_2 frost point. The complex caldera topography of Arsia Mons is shown to substantially influence local pressure distributions, wind velocities, and thermal gradients. Notably, surface temperatures at sites identified by CaSSIS for frost presence exceed the CO_2 frost point by approximately 60 K, suggesting the predominance of H_2O ice in these frost deposits.

https://doi.org/10.1038/s41561-024-01457-7

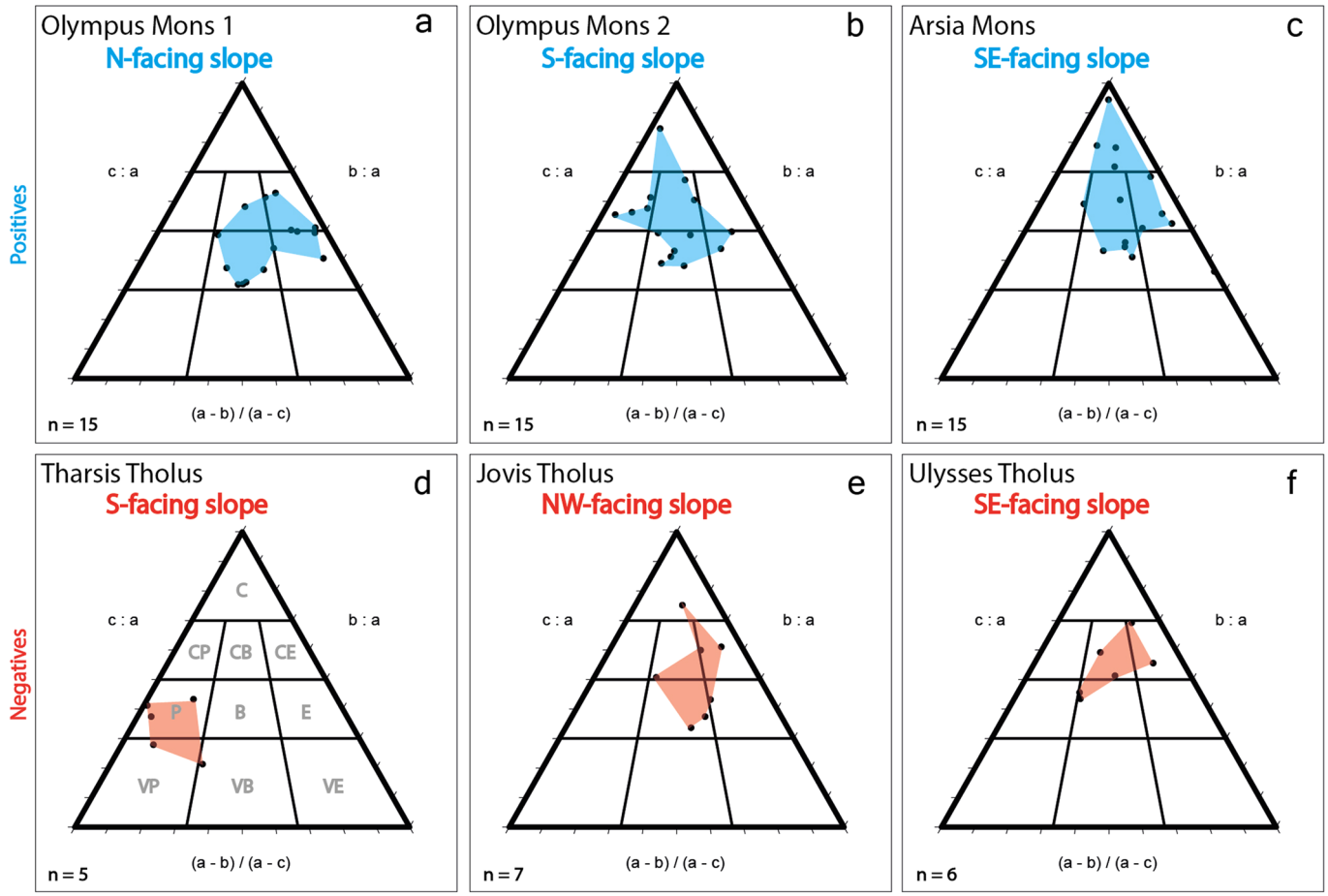

Extended Data Fig. 8 | Triangular (ternary) diagrams of boulder shape across six sites of interest. Boulder shape and size analysis for Olympus Mons (**a**,**b**), Arsia Mons (**c**), Tharsis Tholus (**d**), Jovis Tholus (**e**), and Ulysses Tholus (**f**). The slope aspect of each site is indicated on the respective panel. The Olympus Mons (**a**,**b**) and Arsia Mons (**c**) sites were found to feature a distinct early morning frost signature (positives, blue), the other three sites not (negatives, red) (**d**–**f**) – yet there is no obvious difference in boulder shape across those sites (the colored polygons underline the distribution of points). C = compact, P = platy, B = bladed, E = elongated, V = very; **a** = longest boulder dimension, **b** = intermediate boulder dimension, **c** = smallest boulder dimension. HiRISE image IDs (**a**–**f**): ESP_014275_1990_RED, ESP_043272_1980_RED, ESP_047439_1990_RED, PSP_009884_1980_RED, ESP_057843_1715_RED, ESP_012612_1940_RED, ESP_033711_1985_RED, and ESP_045619_1835_RED.